Erosion and Performance Scaling of Electrodeless Plasma Thrusters with a Magnetic Nozzle

Sungyoung Ha

A thesis
submitted in partial fulfillment of the
requirements for the degree of

Master of Science

University of Washington

2021

Reading Committee:

Justin Little, Chair

Uri Shumlak

Program Authorized to Offer Degree:
Aeronautics and Astronautics

University of Washington

Abstract

Erosion and Performance Scaling of Electrodeless Plasma Thrusters with a Magnetic Nozzle

Sungyoung Ha

Chair of the Supervisory Committee:
Assistant Professor Justin Little
Aeronautics and Astronautics

The scaling of erosion and performance characteristics of electrodeless plasma thrusters with magnetic nozzles is investigated analytically and numerically. A quasi 1-D, two species model was used in conjunction with sheath and sputtering models to develop a numerical scheme for erosion rates and thruster performance. Analytical scaling laws were derived for thrust efficiency and erosion rates and analyzed through the numerical model. Wall impulse, which is derived as the total impulse obtained per unit thickness of wall material eroded, was analyzed as an objective metric for lifetime characteristics. Scaling laws strongly depended on the dominant diffusion mechanism, and the inclusion of anomalous transport introduced unique trade-offs between thrust efficiency and wall impulse. Generalized asymptotic scaling laws for thrust efficiency and wall impulse were calculated for argon and xenon. Comparison with wall impulse of existing Hall thrusters suggest that the erosion rates in electrodeless plasma thrusters can be comparable to those of Hall thrusters and lifetime limitations cannot be ignored.

In addition to the investigation of scaling laws, an EXB probe, or Wein filter, was designed and made as a diagnostic method for future research. The probe was tested on the SPACE Lab Alternative Propellant ECR eXperimental (APEX) thruster along with a

Langmuir probe. The probe was able to collect velocity data as expected and was also able to distinguish doubly charged ions at high input powers. Direct correlation between the numerical model and measured data was not possible likely due to differences in geometry and energy injection methods.

TABLE OF CONTENTS

LIST OF FIGURES

Nomenclature

α_w	Momentum accommodation constant for wall recombination
$\dot{m}$	Propellant mass flow rate
ϵ_c	Energy loss per ion pair created
γ_e	Ratio of specific heats of electrons
ν_e	Electron collision frequency
ν_{er}	Erosion rate
ω_{lh}	Lower hybrid frequency
B	Magnetic field strength
C_s	Ion sound speed
e	Elementary charge
F	Total thrust
g_0	Gravitational acceleration
h_R	Axis to wall plasma density ratio
I_w	Wall impulse

I_{sp}	Specific impulse
L	Length of source channel
m_e	Electron mass
m_i	Ion mass
n_0	Plasma density at axis
n_n	Neutral density
n_z	Radially averaged plasma density
P	Input power
R	Radius of source channel
r	Radial position
R_{in}	Ion neutral momentum exchange rate
R_{ion}	Ionization rate
r_{Le}	Electron Larmor radius
r_{Li}	Ion Larmor radius
T_e	Electron temperature
T_i	Ion temperature
z	Axial position

ACKNOWLEDGMENTS

First, I would like to thank my advisor, Professor Justin Little, for the support throughout my time at the University of Washington. Your kind advice, academic or otherwise, have taught me many things over the last few years and made my masters worth every while. I am grateful for your support and encouragement that made this possible.

I would also like to thank Professor Uri Shumlak. Your lectures on plasma were both clear and informative, and made it possible for me to gain the fundamentals needed to study plasmas. I am sure the time spent in your classes will be invaluable when I find myself in front of the blackboard.

I would like to offer special thanks to Eliot George and Professor Owen Williams. Eliot, you were always available with great advice on any engineering problem, and I appreciate making the jobs of GSAs much easier than it could have been. Owen, thank you for the support and patience through the calibration project, and for supporting me in my career.

I was fortunate to have great labmates throughout my time at the SPACE Lab. Curtis, thanks for putting up with all my bad jokes and for the lunch breaks. Peter, you were one of the best people to grab a drink with. Charlie, your attention to organization and projects were inspirational. Anna, you deserve special thanks for letting me nag you for thruster measurements and working with me to figure out issues with the EXB probe. Your laughter never failed to brighten the mood. Arvindh, Wes, and Jonah, thank you for being good friends throughout my time here. Special thanks to Danny, who helped with machining parts for the EXB probe. To all the new lab members, I wish global circumstances had been better and I wish you good luck.

DEDICATION

to my parents, and God.

Chapter 1

INTRODUCTION

Electrodeless plasma thrusters, along with magnetic nozzles, are actively being researched as an innovative propulsion method [1][2]. These types of thrusters can operate in a wide range of powers ranging from $< 50W$ Electric Cyclotron Resonance (ECR) thrusters [3] and Helicon thrusters [4] to $> 50kW$ Helicon thrusters [5], largely due to the absence of electrodes whose erosion typically limits the lifetime of high power thrusters [6]. The quasineutral nature of the plume does not require it to have an additional neutralizer cathode, along with the associated weight and complexity. It is also possible to use in-situ alternative propellants such as water, which may contaminate and corrode the electrodes of other types of thrusters [7][8].

Having such benefits, it is no surprise that there is an abundance in both theoretical and experimental work on the design and performance of such thrusters and Magnetic Nozzles (MN). However, the erosion and lifetime characteristics of these thrusters are rarely evaluated in literature, perhaps due to the fact that the electrodeless nature gives the impression that lifetime limitations are less relevant and that these are yet to see active in-flight testing. While it is true that there are no electrodes, channel wall erosion in the plasma source area induced by accelerated ions across the plasma sheath may still be significant. In this thesis, the scaling of erosion characteristics in MN thrusters will be theoretically investigated by combining preexisting physical models into a numerical scheme. Along the way, the scaling of other performance factors such as thrust efficiency will be revisited to identify any new trade-offs or design considerations that may be of interest.

1.1 Classification of thrusters

Before establishing the problem, it is necessary to identify the scope of this thesis. One way to classify thrusters with magnetic nozzles is by their driving species [6]. In magnetic nozzles, the species with the highest temperature drives the plasma expansion. Thrusters that satisfy $T_i \gg T_e$ are driven by ions, and utilize mechanisms such as ion cyclotron resonance to heat the ions [9][10]. Thrusters that satisfy $T_e \gg T_i$ are driven by electrons, and are the main focus of this thesis. It should also be noted that non-steady state thrusters such as Pulsed Inductive Thrusters (PIT) will not be discussed.

The two most commonly discussed thrusters in this category are the Helicon Plasma Thruster (HPT) and Electron Cyclotron Resonance Thruster (ECRT). The HPT utilizes a helicon plasma source to generate and heat the plasma. A helicon plasma source operates by using a steady state magnetic field to propagate helicon waves into the plasma [11]. This method allows high coupling efficiencies and ionization rates since the waves can penetrate deep into the plasma. Combined with the fact that the magnetic field can be axially oriented to form a magnetic nozzle, it is an attractive candidate for a thruster mechanism. The ions are accelerated by either the formation of double layers, which in this case the thruster is called a Helicon Double Layer Thruster (HDLT) [12][13], or by ambipolar electric fields caused by the expansion of electrons with higher mobility [14]. The main difference between the two mechanisms lie in the length of the potential drop in the plume, where double layers are typically on the order of ten or hundred debye lengths, whereas ambipolar acceleration occurs more gradually along the magnetic nozzle.

An Electron Cyclotron Resonance Thruster (ECRT) utilizes the absorption of whistler waves in the electron cyclotron resonance region when propagating from high to low magnetic fields. The microwave is transmitted to the plasma through a waveguide or coaxial antenna. Similar to the HPT, the heated electrons expand out of the thruster and magnetic nozzle, creating an ambipolar electric field which accelerates the ions.

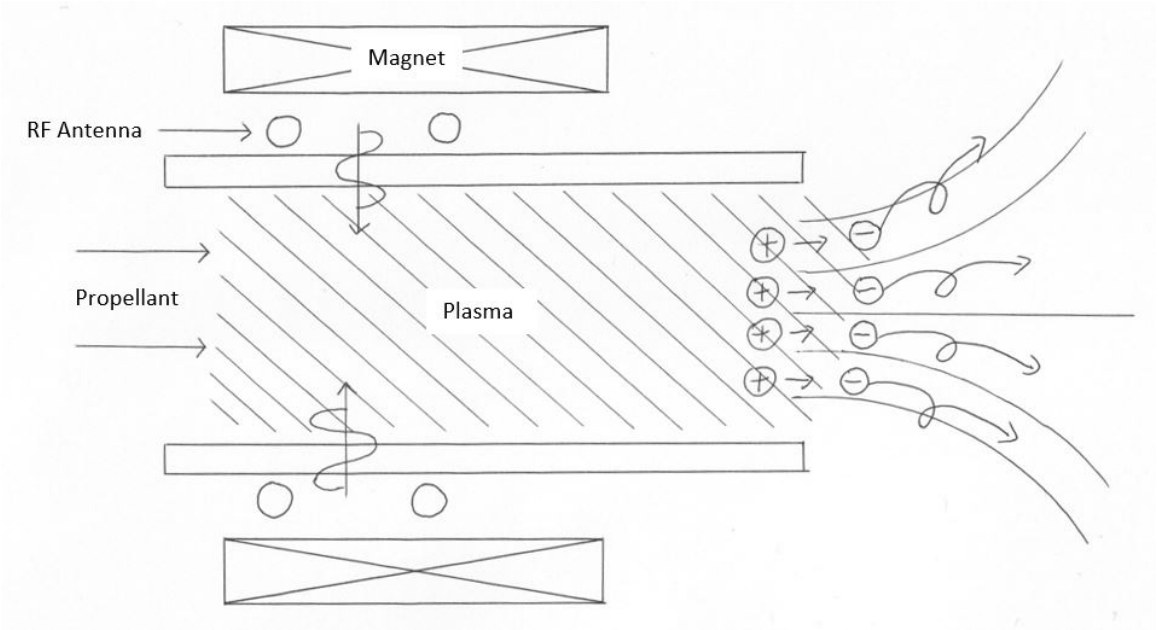

Figure 1.1: Schematic of a Helicon Plasma Thruster. Figure adapted from [1].

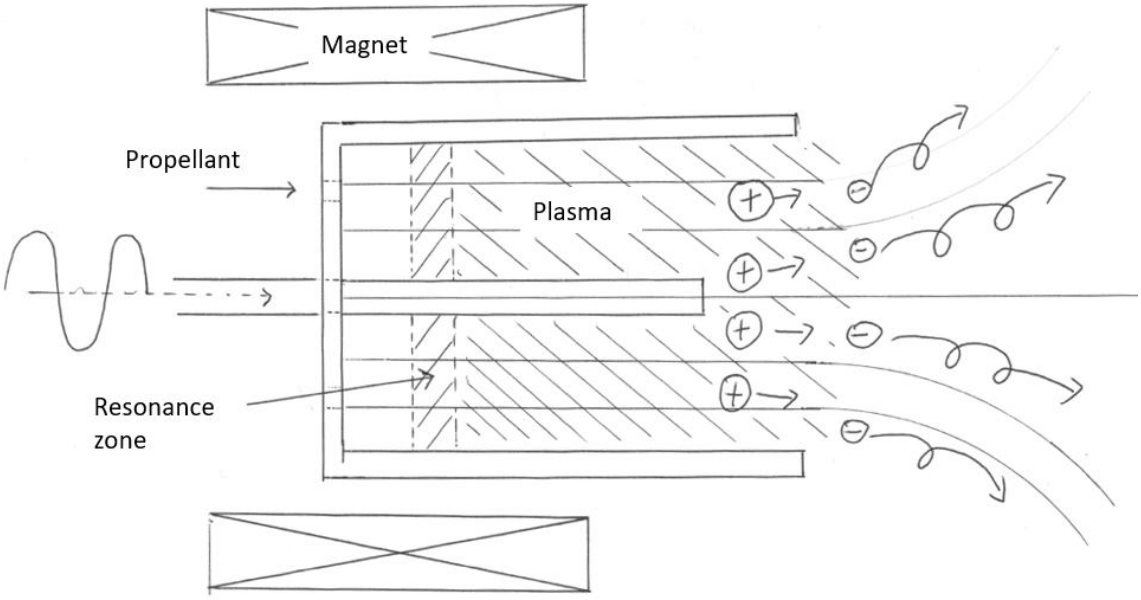

Figure 1.2: Schematic of an ECR Thruster with a coaxial antenna. Figure adapted from [1].

1.2 Literature review

In this section, we will touch upon literature related to the lifetime analysis and erosion of electrodeless thrusters as well as the physical model inside the source channel. Literature related to sheath or erosion physics will be discussed in the relevant sections. One of the few literature that discusses erosion comes from Berisford *et al.*, where the wall etching in a helicon plasma source with a cylindrical geometry was experimentally confirmed by placing strips of kapton tape along the inside of the source tube [15]. Erosion of the kapton sample was observed in the regions directly under the antenna strips, while kapton was deposited in other areas, which the authors conclude that the erosion occurs due to the acceleration caused by the local electric field of the antenna, and erosion does not take place elsewhere. While this work highlights the possibility that erosion may be enhanced in the vicinity of the antenna, the validity of the results in a thruster application is debatable. The source tube was made of glass and the operation time of the plasma source was approximately 30 minutes, which is too short to observe wall erosion associated with thruster lifetime.

Del Valle *et al.* proposed an experimental framework to characterize dielectric wall erosion in HPTs, specifically the VASIMIR thruster [16]. In addition to an experimental setup, the work gives a outline of how erosion characteristics may be theoretically estimated. The simplified model is given in three steps: i) Plasma Ionization, ii) Ion Radial Diffusion, and iii) Plasma-Wall Interaction. Unfortunately, no experimental results from an extended thruster operation could be found in literature.

Some of the earliest physical models of a HPT were formed by Fruchtman [17][18][19]. Fruchtman devised a performance model for both collisionless and collisional thrusters, and predicted that ionization and backwall losses were the primary source of inefficiencies. In these models, Fruchtman does not include radial losses. A more complete model that includes radial losses, ionization, recombination and magnetic nozzle performance was derived by Ahedo and Navarro Cavallé [20]. They showed that a high enough magnetic field and

electron temperature is required for high propellant utilization rates and minimal wall losses. However, experimental results show significantly lower efficiencies predicted by this model [21][22][23]. The reason for this discrepancy is not yet completely understood, however the fact that this model assumes a classical diffusion mechanism can be one factor. Using similar methods and approximations, Lafleur derives a performance model for HPTs by adopting a semi-empirical diffusion constant by fitting a Bohm-like diffusion function to experimental results in literature [24]. In this model it is shown that radial losses can be significant.

1.3 Impact of this work

This thesis intends to provide an initial estimation on the erosion of electrodeless MN thrusters through combining physical models that have been successfully used in the past. General scaling laws for erosion will be derived, as well as for other performance metrics. The most common metrics of an electric propulsion system are thrust efficiency η_T and specific impulse I_{sp} which are defined as:

$$\eta_T \equiv \frac{F^2}{2\dot{m}P}, \tag{1.1}$$

$$I_{sp} \equiv \frac{F}{\dot{m}g_0}, \tag{1.2}$$

where F is the thrust, P is the total input power, g_0 is the gravitational acceleration at sea level, and $\dot{m}$ is the propellant mass flow. In addition to these, a performance metric for erosion is proposed, which is defined as

$$I_W \equiv \frac{F}{\nu_{er}}, \tag{1.3}$$

where ν_{er} is the maximum erosion rate of the channel wall in mm/s. This metric has the physical meaning of total impulse obtainable per unit thickness of wall material. While it is

true that this parameter will change over the course of the thruster lifetime due to possible changes in geometry, it allows the erosion characteristics to be compared over different thrusters in a consistent manner. This has advantages over lifetime measurements in hours, since such assessments do not represent actual physical properties, and the values depend on the specific type of thruster. Through this process, this thesis intends to supplement the lack of literature on the erosion of electrodeless plasma thrusters by deriving and analyzing scaling laws which can be related to future experimental results.

Chapter 2

PHYSICAL MODEL

The goal of this chapter is to review the physical models found in literature, and formulate a combined model that obtains the plasma parameters and performance characteristics given a set of operating conditions. The models will be separated into three parts: i) the plasma channel model, ii) the sheath model, and iii) the sputtering model. This method and structure of erosion estimation can be found in literature on Hall thruster erosion [25][26], where the specific physical models implemented differ from reference to reference. In the following sections, the models chosen in this analysis are explained along with the reasons behind the decisions.

2.1 Plasma channel model

The physical model inside the source tube of a electrodeless thruster have been disscussed in multiple sources, which utilize similar assumptions and geometries. Early work by Fruchtman [17][18][19] forms a two-species (electrons and singly charged ions), 2-D model in a cylindrical geometry. Throughout the source channel, the plasma is assumed to be quasineutral and to have a constant electron temperature T_e. The particle motion is given as a set of simplified differential equations from particle and momentum conservation laws, and solved while assuming perfect plasma confinement. Asymptotic scaling laws are derived and compared to experimental results available at the time. A similar, but more rigorous model was derived by Ahedo and Navarro Cavallé [20]. In this model, wall recombination and electron inertial effects are included in the axial and radial conservation equations. Spatial density and velocity profiles and neutral dynamics are discussed, as well as more detailed analysis

of the magnetic nozzle. Lafleur proposed a similar quasi 1-D model using a semi-empirical approach to the radial diffusion constant [24]. In this model, experimental results of center to edge density ratios are fitted to a Bohm-like diffusion constant and applied to a similar scheme to Ahedo and Navarro Cavallé. The magnetic nozzle model is assumed such that detachment occurs when the ion larmor radius equals the radius of the plume. In all models, the power coupling efficiency between the rf waves and plasma is not modeled and kept as unity or a constant.

The plasma channel model mostly follows the derivation by Ahedo and Navarro Cavallé [20], but with a modified radial diffusion rate to include the effects of anomalous transport. Taking a different approach to Lafleur's semi-empirical approach [24], the contribution of anomalous Bohm-like diffusion is kept as a variable to observe the scaling in different situations, and to keep the analysis relevant to a wide range of potential future experiments. For this analysis, we consider a cylindrical plasma source channel as in Figure 2.1. The magnetic field is assumed to be purely axial and constant throughout the channel. Under these conditions, the physical properties inside the source channel can be described with five variables: the magnetic field strength B, channel radius R, channel length L, propellant mass flow rate $\dot{m}$, and the input power P. These are the main variables this work will use to observe the scaling of thruster performance and erosion.

To formulate the conservation equations, it is necessary to further specify the assumptions for the plasma. Following the assumptions in reference [20] and [24], the assumptions can be summarized as follows.

i) All parameters are axially symmetric.

ii) The electron temperature T_e is constant within the source channel.

iii) Cold ions and neutrals, i.e. the ion and neutral pressure is small compared to the electron pressure. The ion temperature is assumed to be $0.2eV$ in the numerical scheme.

iv) The plasma is quasineutral throughout the source channel outside of the plasma

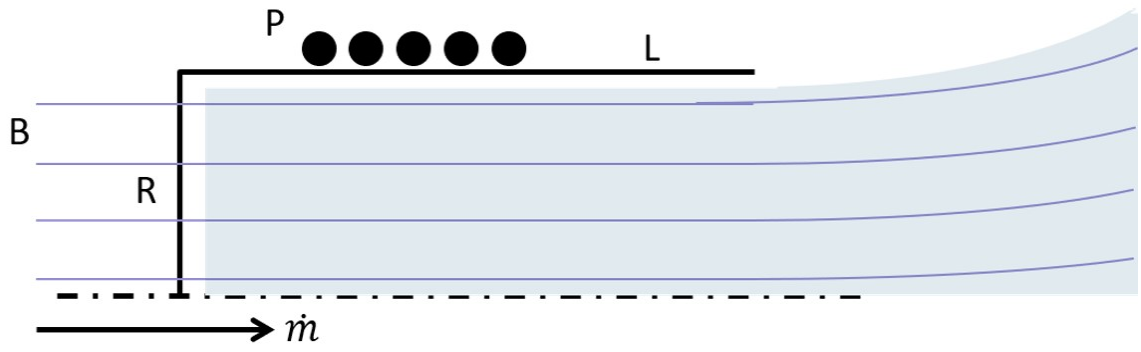

Figure 2.1: Geometry of source channel.

sheath near the walls.

v) The walls are dielectric, i.e. the net current through the walls are zero.

vi) Plasma density is radially self-similar throughout the channel and has the form of $n(z,r) = n_z(z)n_r(z,r)$ where $(2/R^2)\int_0^R rn_r dr = 1$ for all z.

vii) Neutral density is radially constant and expressed as $n_n(z)$.

viii) Axial electron inertia is negligible.

ix) Neutrals are injected at $320m/s$ into the channel, which is near the sound speed [24]. Neutral characteristics will be discussed in more detail, but this assumption is mostly relevant in the context of numerical implementation and not the scaling laws.

x) Only singly charged ions are considered.

xi) The magnetic effects on the ions are negligible, i.e. the ion larmor radius $r_{Li} \ll R$.

The axial conservation equations are as follows.

$$n_z u_z + n_n u_n = \frac{\dot{m}}{m_i \pi R^2} \equiv \Gamma_0, \tag{2.1}$$

$$\frac{\partial}{\partial z}\left(n_z u_z\right) = n_z\left(n_n R_{ion} - \nu_w\right), \tag{2.2}$$

$$u_z \frac{\partial u_z}{\partial z} = -C_s^2 \frac{\partial \ln\left(n_z\right)}{\partial z} - n_n\left(R_{in} + R_{ion}\right)\left(u_z - u_n\right), \tag{2.3}$$

$$u_n \frac{\partial u_z}{\partial z} = -n_z\left[R_{in}\left(u_n - u_z\right) + \frac{\nu_w}{n_n} u_n\left(1 - \alpha_w\right)\right], \tag{2.4}$$

$$e\frac{\partial \phi_z}{\partial z} = T_e \frac{\partial \ln\left(n_z\right)}{\partial z}. \tag{2.5}$$

Equations 2.1 to 2.5 describe continuity, ionization, ion momentum, neutral momentum, and electron momentum, respectively. It is implied that the plasma density follows the expression $\langle n(z,r) f(r/R)\rangle = \beta n_0(z) = n_z$, which is consistent with the assumptions made. We can also write the radial conservation equations, which are as follows [20].

$$\frac{1}{r}\frac{\partial}{\partial r}\left(r n_r u_r\right) = n_r \nu_w \tag{2.6}$$

$$u_r \frac{\partial u_r}{\partial r} = -C_s^2 \frac{\partial \ln n_r}{\partial r} - \frac{eB_0}{m_i} u_\theta - n_n\left(R_{in} + R_{ion}\right) u_r, \tag{2.7}$$

$$u_r \frac{\partial u_\theta}{\partial r} = \frac{eB_0}{m_e} u_r - \left[n_n\left(R_{en} + R_{ion}\right) + n_r R_{ei}\right] u_\theta - \frac{u_\theta u_r}{r}, \tag{2.8}$$

$$e\frac{\partial \phi_r}{\partial_r} = T_e \frac{\partial \ln n_r}{\partial r} + eB_0 u_\theta - m_e \frac{u_\theta^2}{r}. \tag{2.9}$$

For the purpose of this work, we are interested in the plasma flux to the channel walls. The boundary condition is that the ions enter the wall sheath at the ion sound speed, which is the Bohm sheath criterion. In the regime where the magnetic field strength is large enough such that $\omega_{lh} = \frac{eB}{\sqrt{m_i m_e}} \gg \frac{R}{C_s}$, the plasma flux to the wall is derived as

$$\Gamma_{wall} = n_0(z) a_0 J_1(a_0) \hat{\nu_e} / \hat{\omega_{lh}}^2, \tag{2.10}$$

where a_0 is the first zero of the Bessel function of the zeroth kind, J_1 is the Bessel function of the first kind, $\hat{\omega_{lh}^2} = \omega_{lh} R / C_s$ is the normalized lower hybrid frequency, and $\hat{\nu_e} = \Sigma \nu_e R / C_s$ is the normalized electron collision frequency. ν_e implies electron collision frequencies including ion-electron and neutral-electron collisions [20]. To include the effect of anomalous Bohm-like diffusion, the Bohm collision frequency is defined as $\nu_{eb} = \Omega_e / 16$ where Ω_e is the electron gyrofrequency. Hence $\Sigma \nu_e = \nu_{ei} + \nu_{en} + a_B \nu_{eb}$ where $0 \leq a_B \leq 1$ is the Bohm ratio describing the amount of contribution of anomalous transport. The Bessel function-like solution for the radial profile also determines the value of the radial density average $\beta \approx 1/2.3$ [27], which will be assumed for the remainder of the analysis.

To assist in the analysis, it is useful to define a parameter $h_R \equiv n(z, R)/n(z, 0)$ which is the ratio between the plasma density at the radial sheath boundary and the density at the axis. Nomenclature is adopted from Lafleur [24]. From equation 2.10 and the expression for electron collisions, it is possible to derive that in the case of purely classical diffusion $h_R \propto \frac{n}{B^2 R T_e} \propto \frac{\dot{m}}{B^2 R^3 T_e^{3/2}}$ and in the case of purely bohm diffusion $h_R \propto \frac{T_e^{1/2}}{BR}$. These scaling laws directly relate to the scaling of radial losses, and hence with performance criteria which will be discussed in chapter 3.

Now that the radial characteristics have been defined, it is possible to revisit equations 2.1 through 2.5 to formulate a numerical scheme. To further simplify the set of equations, it is reasonable to assume $|u_z| \gg |u_n|$, and $R_{ion} \gg R_{in}$ for most cases [27]. While the assumption of $|u_z| \gg |u_n|$ becomes invalid in some region within the channel where $u_z \approx 0$, the neutral velocity is generally much slower than the ion sound speed and the neutral density is low for ideal operating ranges. Therefore, this approximation can be applied without significantly affecting scaling or performance characteristics. For the range of electron temperature typically observed in these thrusters, R_{ion} is typically orders of magnitude higher

than R_{in}. The momentum accommodation constant α_w demonstrates how much of the axial ion momentum is maintained when it undergoes wall recombination and re-injected into the neutral stream, where $\alpha_w = 0$ means the ions are completely halted. The specific value of α_w may be affected by wall material, ion mass, incidence angle, and other parameters, but in the pressure regimes of thruster operation incident gas particles are mostly reflected diffusely, hence $\alpha_w \approx 0$ [28]. Combined with the assumption that $|u_z| \gg |u_n|$, we can assume $1 - \alpha_w \approx 0$, effectively stating that the neutral velocity is constant within the source channel.

With the approximations applied, the axially dependent parameters can be expressed in a set of normalized ordinary differential equations [27].

$$\frac{d\hat{u}_z}{d\zeta} = (1 - \hat{u}_z\hat{n}_z)\left(1 + \hat{u}_z^2\right) - \hat{\nu}_w, \tag{2.11}$$

$$\frac{d\hat{n}_z}{d\zeta} = -\left(2\left(1 - \hat{u}_z\hat{n}_z\right) - \hat{\nu}_w\right)\hat{u}_z\hat{n}_z, \tag{2.12}$$

$$\frac{d\hat{z}}{d\zeta} = 1 - \hat{u}_z^2. \tag{2.13}$$

The parameters are normalized such that $\hat{u}_z = u_z/C_s$, $\hat{n}_z = n_z C_s/\Gamma_0$, $\hat{\nu}_w = \nu_w u_n/R_{ion}\Gamma_0$, and $\hat{z} = z/L$. The boundary conditions that are imposed to solve these equations are

$$\hat{u}_z = 1, \hat{n}_z = \eta_d, \hat{z} = 0, \tag{2.14}$$

at the thruster exit where $\eta_d \equiv \dot{m}_i/\dot{m}$ is the propellant utilization rate defined as the ratio between the ion flow rate out the thruster and the propellant mass flow rate. The integration ends when $\hat{u}_z = -1$ which is the Bohm sheath criterion at the backwall. At this point, the equation is fully solvable given T_e, B, R, L, and $\dot{m}$.

To complete the physical model and analyze power characteristics, it is necessary to form a power conservation equation that relates electron temperature to input power.

$$P = P_{backwall} + P_{exit} + P_{wall}, \tag{2.15}$$

$$P_{backwall} = \pi R^2 e n_z(-L) C_s \left(\left(\frac{5}{2} + \frac{1}{2} \ln \left(\frac{m_i}{2\pi m_e} \right) \right) T_e + \epsilon_c \right), \tag{2.16}$$

$$P_{exit} = \pi R^2 e n_z(0) C_s \left(\left(\frac{1}{2} + \frac{1}{\gamma_e - 1} \right) T_e + \epsilon_c \right), \tag{2.17}$$

$$P_{wall} = 2\pi R e C_s \int_{-L}^{0} n_z(z, R) dz \left(\left(\frac{5}{2} + \frac{1}{2} \ln \left(\frac{m_i}{2\pi m_e} \right) \right) T_e + \epsilon_c \right). \tag{2.18}$$

Here, ϵ_c is the loss per ion pair collisions and γ_e is the ratio of specific heat for electrons. The values for R_{ion} were taken from reference [29] and ϵ_c were taken from references [30] (argon), [31] (krypton) and [32][33] (xenon). Here, the magnetic nozzle is assumed to be ideal where the electrons expand polytropically throughout the plume, depositing all its thermal energy into the kinetic energy of the ions. The velocity gain of the magnetic nozzle is then calculated as $g_u = \sqrt{\frac{\gamma_e+1}{\gamma_e-1}}$ where $\gamma_e \approx 1.2$ is used which is the approximate value observed from magnetic nozzle experiments [34][7]. Figure 2.2 illustrates the numerical process of solving the plasma channel model. The full numerical process involves two major iterations, where one is to find the propellant utilization rate corresponding to the electron temperature and thruster length, and the other is to iterate this process to match the electron temperature with the input power. In the analysis, scaling is observed by setting the electron temperature as a parameter instead of the input power because electron temperature relates more directly with performance metrics such as specific impulse, and it allows the power matching iteration to be omitted, significantly reducing the computational burden associated with nested loops. Figure 2.3 shows an example solution of the plasma density and velocity profile within the source channel. It can be seen that there is a region in the channel where the density is maximum, which corresponds to where the plasma velocity is zero. The plasma is assumed to be 'choked' at the channel exit, which is valid for

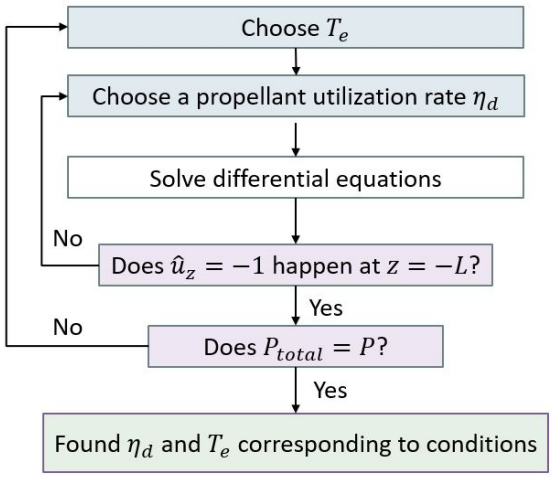

Figure 2.2: Process of solving the plasma channel model.

most magnetic nozzle configurations and the range of operations this work is interested in. However, it is possible for the numerical solution to become invalid in extreme conditions where these boundary conditions cannot be satisfied.

The validity of this model for non-helical plasma thrusters such as ECRTs are somewhat up for debate, as the differences in coupling mechanisms may induce local differences in plasma properties, most notably electron temperature. Especially in ECRTs with a center antenna, simulations report a possibly significantly higher electron temperature around the antenna and in the resonance region [35]. In this case, erosion can be much more prominent at the center pole wall due to larger sheath potential drops and local electric fields. Due to the lack of data, it is difficult to confirm and model such phenomena. However quasi-1D models like this have been used in past literature to analyze ECRTs [7][36]. While this study generalizes the analysis to electrodeless thrusters with magnetic nozzles, it is possible that different types of thrusters show unexpected localized behaviour in practice.

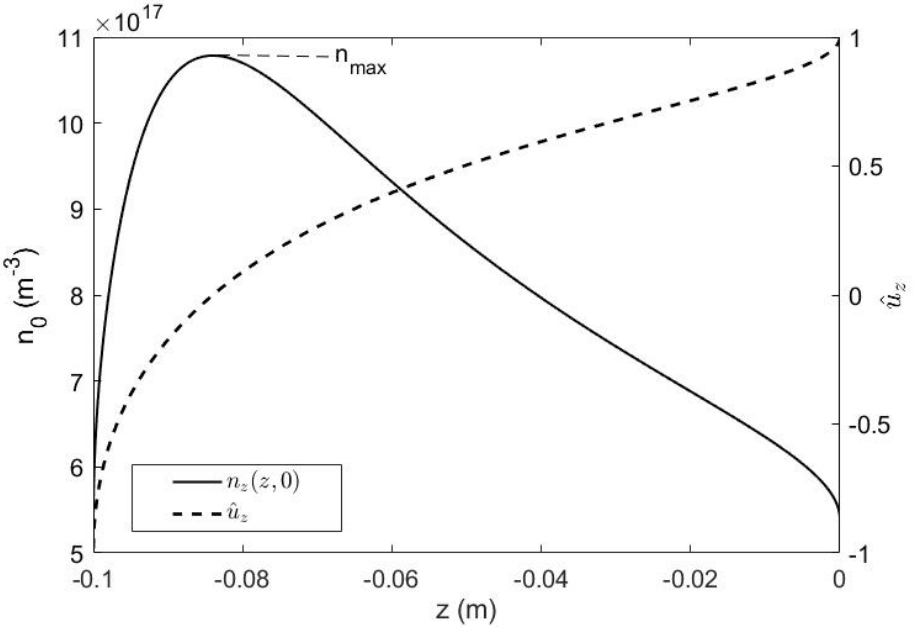

Figure 2.3: Sample profile of axial plasma density and mach number with the conditions of B = 1kG, R = 5cm, L = 10 cm, T_e = 25 eV, $\dot{m}$ = 1 mg/s, argon propellant.

2.2 Sheath model

The sheath model is necessary to evaluate the energy gained by the ions when they are accelerated across the plasma sheath formed at the walls. The sheath structure, especially in the presence of a magnetic field is studied in multiple references, most notably from the work of Riemann [37][38][39] and Chodura [40]. The presheath - sheath matching problem that is used to analyze the sheath structure considers how the collisional presheath area and the non-collisional sheath area are seamed together. Beilis [41][42] and Keidar [43] proposed a smooth presheath - sheath matching model in the presence of an oblique magnetic field, and Ahedo [44] investigated the effect of secondary electrons in the sheath structure. In the perspective of erosion, the energy gain of the ions accelerated across the sheath and how it may be affected by the magnetic field is the main interest. Holland *et al.* derives the sheath potential in the presence of a oblique magnetic field with a small angle of incidence $\epsilon < 10^{\circ}$

using a fluid model [45]. In this reference, the potential at the wall is derived as

$$\frac{\Phi_w}{T_e} = \frac{1}{2}\ln\left(\frac{2\pi m_e}{m_i}\right) + \frac{v_{Ew}^2}{v_{te}^2}\cos\epsilon^2, \tag{2.19}$$

where v_{Ew} is the $E \times B$ drift velocity at the wall, v_{te} is the thermal velocity of the electrons, and ϵ is the incident angle of the magnetic field. Typically $v_{Ew} \ll v_{te}$, hence the magnetic field dependent term is negligible. Chodura also arrives at the conclusion that the wall potential is nearly independent of the magnetic field strength and angle of incidence for all incidence angles of $10^\circ < \epsilon < 90^\circ$. Therefore the potential drop across the plasma sheath can be approximated as the case of a saturated sheath without a magnetic field. Considering the boundary condition in this derivation is that the ions are entering the sheath parallel to the magnetic field at the ion sound speed, the total energy of the ion when it impacts the wall can be expressed as

$$E_{ion} = \frac{T_e}{2}\left(1 + \ln\left(\frac{m_i}{2\pi m_e}\right)\right). \tag{2.20}$$

The boundary condition of the sheath model that the ions enter the sheath parallel to the magnetic field at the sound speed may seem inconsistent from the bohm sheath criterion imposed in the plasma channel model. However, there is a point in the plasma sheath where the ion velocity perpendicular to the wall becomes the sound speed, which resolves the inconsistency in flux. In addition, the sheath thickness is small compared to the channel radius. The sheath model is only used to evaluate the potential energy gain of the ions, hence the specific location of the presheath - sheath boundary has negligible impact on the analysis. It should be noted that secondary electron emissions are not considered in this analysis.

2.3 Sputtering model

Earliest work on sputtering caused by ion impingement have been done by Sigmund [46]. Sigmund formulates a general sputtering model based on linear cascade theory. Expanding on this work, Bohdansky derives a universal relation for sputtering yield [47]. Yamamura and Tawara modifies the expression of Bohdansky through empirical data of various ion-material combinations [48].

For this analysis, the expression in Lieberman [49], which is adopted from Zalm [50] is used. This is the approximation also used by Berisford *et al.* in their estimation of wall erosion in a helicon plasma source [15]. The expression for sputtering yield in atoms per ion is given as

$$Y \approx \frac{0.06}{\epsilon_t}\sqrt{\bar{Z}_t}\left(\sqrt{E_{ion}} - \sqrt{\epsilon_{thr}}\right), \tag{2.21}$$

where

$$\bar{Z}_t = \frac{2Z_t}{(Z_i/Z_t)^{2/3} + (Z_t/Z_i)^{2/3}}. \tag{2.22}$$

Here, Z_t is the atomic number of the target material or wall material, Z_i is the atomic number of the incident ion, ϵ_t is the surface binding energy, and ϵ_{thr} is the threshold energy. The threshold energy can be approximated by

$$\epsilon_{thr} \approx 8\epsilon_t \left(\frac{m_i}{m_t}\right)^{2/5}, \tag{2.23}$$

where m_i and m_t are the mass of the incident ion and target respectively [51]. For the analysis, we choose BN as the wall material, which is a commonly used material in electric propulsion applications. The difficulty in estimating the erosion properties of BN comes from its lattice structure, which can exhibit different behavior compared to monatomic materials. Therefore a semi-empirical approach is adopted where the experimental data

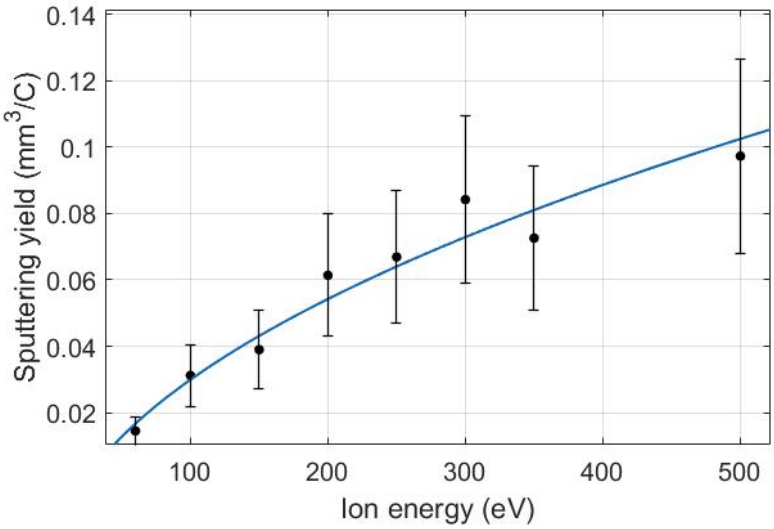

Figure 2.4: Sputtering yield fit (line) of HBC BN to experimental data of Rubin *et al.*(dots).

from Rubin *et al.* [52] are fitted to the expression of equation 2.21 using a least squares method.

In the work of Rubin *et al.*, the expressions from Bohdansky[47] and Yamamura[48] are adopted. In this analysis, equation 2.21 is adopted due to its more general expression, where a single fit can be approximated to include the effects of different propellants, whereas the expressions from Bohdansky and Yamamura depend on specific ion-target combinations. From equation 2.20, it can be seen that the velocity gained in the sheath can be several times the ion sound speed for typical electron temperature ranges. Therefore it is approximated that the ions have normal incidence to the wall. Figure 2.4 shows the least squares fit. The density of BN was taken as $2.1 g/cm^3$, and $m_t \propto 2Z_t$ was assumed for the conversion between the sputtering yield units. The threshold energy $\epsilon_{thr} \approx 24eV$ was also taken from Rubin *et al.* The fit yields $Z_t \approx 6.99$, which is consistent with the chemical composition of BN, and is used throughout the analysis in the form of equations 2.21 - 2.23.

Chapter 3

SCALING LAWS

In this chapter, the physical model discussed in chapter 2 are used to derive asymptotic scaling laws, and are compared to numerical results. The typical range of parameters observed in these type of thrusters are listed in table 3.1. Although these do not cover the entirety of possible values, they give a range wide enough to observe scaling laws and represent the majority of electrodeless thrusters developed.

Parameters	**Range**
B	10 G - 2 kG
R	3 - 6 cm
L	10 cm
$\dot{m}$	1 mg/s
P	50 W - 2 kW
n_z	$10^{18}\ m^{-3}$
T_e	10 - 40 eV
R_{ion}	$1.5 \times 10^{-14} m^3/s$

Table 3.1: Typical range of parameters.

3.0.1 Performance scaling

Before the erosion characteristics are examined, other conventional performance metrics are discussed. The thrust from a thruster with a magnetic nozzle can be expressed as

$$F_T = \pi R^2 g_u \cos\theta_{div} n_z(0) m_i C_s^2 + \dot{m} u_n \left(1 + \frac{eT_g}{m_i u_n^2}\right), \tag{3.1}$$

where $g_u = \sqrt{\frac{\gamma_e+1}{\gamma_e-1}} \approx \sqrt{11}$ is the velocity gain of the ideal magnetic nozzle model, $\theta_{div} \approx 0$ is the divergence of the magnetic nozzle, and T_g is the temperature of the neutrals. In the analysis $T_g \approx 0.026eV$ is set[24], but the contribution of the thermal pressure is small compared to the total neutral thrust. From the definition of thrust efficiency in equation 1.1 and equation 3.1, the thrust efficiency can be decomposed into several efficiencies as follows.

$$\eta_T \equiv \frac{F^2}{2\dot{m}P} = \eta_{div}\eta_d\eta_P\eta_I, \tag{3.2}$$

$$\eta_{div} = \cos\theta_{div}, \tag{3.3}$$

$$\eta_d \equiv \frac{\dot{m}_i}{\dot{m}} = \frac{\pi R^2 C_s n_z(0) m_i}{\dot{m}}, \tag{3.4}$$

$$\eta_P = \frac{P_{exit}}{P}, \tag{3.5}$$

$$\eta_I = \frac{T_e}{T_e + \epsilon_c / \left(\frac{1}{2} + \frac{1}{\gamma_e - 1}\right)}. \tag{3.6}$$

Here, $\eta_{div} \approx 1$ is the divergence of the magnetic nozzle, η_d is the propellant utilization rate, η_P is the power efficiency defined as the ratio of the directed power to the total input power into the plasma, and η_I is the ionization efficiency which describes the losses by ionization and excitation. It should be noted that the power efficiency is different from the coupling efficiency, which is the ratio of total input power to the power absorbed by the plasma and is assumed to be unity for the purposes of this analysis. By breaking down the thrust efficiency into these components, it is possible to form a more detailed picture

of performance scaling. In the following sections, the scaling of each of these individual components are discussed.

First, the propellant utilization rate is discussed. Due to the fact that the expression for the plasma density at the thruster exit is influenced by a variety of factors, it is difficult to formulate a simple algebraic scaling law for η_d. Fruchtman derives the approximation for η_d in the limit where radial losses are ignored and when η_d is large as [19]

$$\eta_d \approx 1 - 2\exp\left(\frac{\dot{m}R_{ion}L}{\pi R^2 m_i u_n C_s}\right). \tag{3.7}$$

In the work of Ahedo and Navarro Cavallé [20], the propellant utilization rate is derived in the case of ideal confinement as

$$\frac{\dot{m}R_{ion}L}{\pi R^2 m_i u_n C_s} = \int_{-\pi/4}^{\pi/4} \frac{1-\tan^2\zeta}{1-\eta_d \sin 2\zeta} d\zeta. \tag{3.8}$$

In both cases, the propellant utilization rate is a function of the dimensionless parameter $\frac{\dot{m}R_{ion}L}{\pi R^2 m_i u_n C_s}$, which can be interpreted as the likelihood of a neutral particle being ionized before leaving the channel. However, radial losses are assumed to be small in both expressions and wall recombination can significantly lower the utilization rate.

Figure 3.1 shows numerical results of η_d compared to the ideal expression of equations 3.7 - 3.8. It can be seen that radial losses significantly affect the propellant utilization rate, which is more pronounced in the case of xenon compared to argon, mainly due to the larger ion larmor radius. The expression of Fruchtman does not agree well with the trend of the results, mostly due to the neglect of radial losses and mathematical approximations made in the derivation. The disparity between the case of full bohm diffusion and purely classical diffusion is particularly important. In literature that adopts a classical diffusion mechanism, a moderate magnetic field strength is enough for the ideal scaling laws to be valid. However, anomalous bohm-like diffusion can quickly dominate over classical diffusion which significantly decreases the maximum propellant utilization rate, and subsequently the

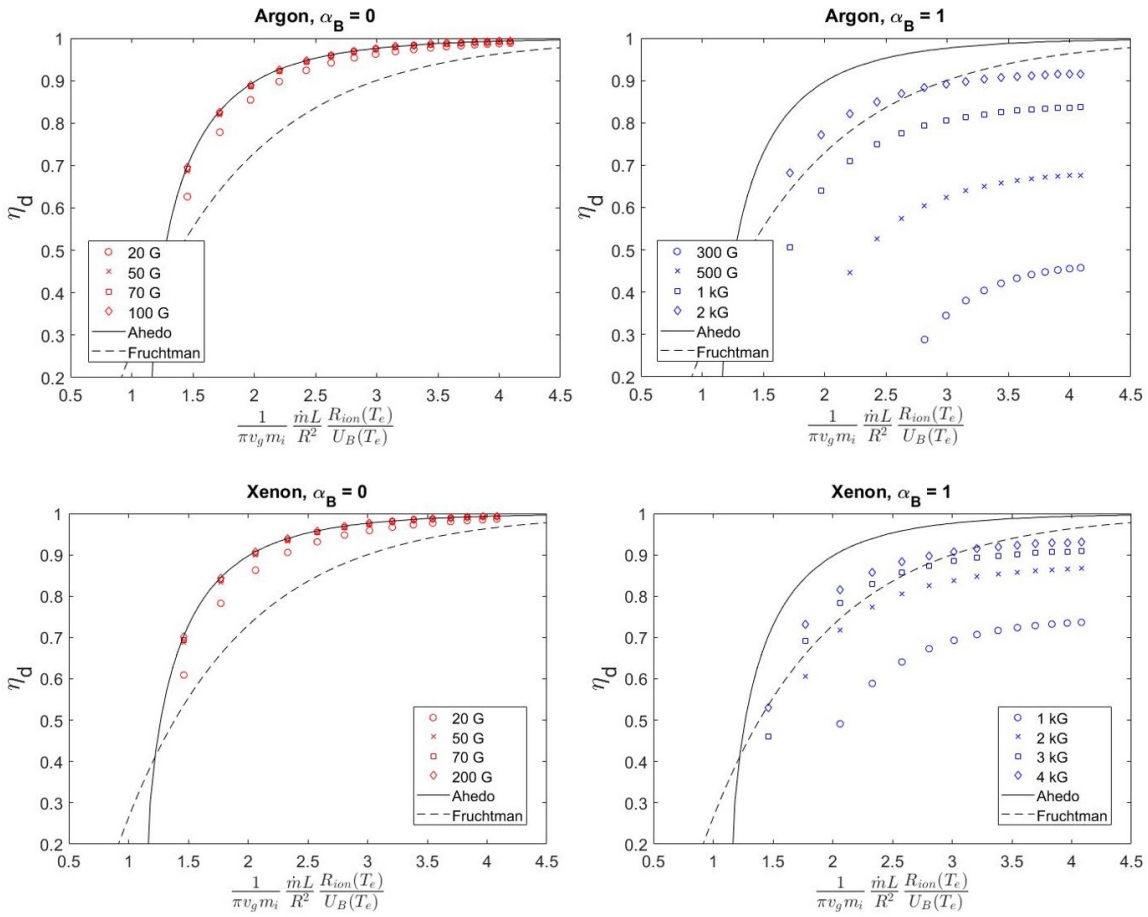

Figure 3.1: Propellant utilization rate scaling with varied magnetic field and T_e. Other parameters are fixed at $R = 5cm$, $L = 10cm$, $\dot{m} = 1mg/s$.

thrust efficiency a thruster can achieve. These results show that evaluating the diffusion mechanism is critical in making an accurate prediction of performance in an experimental setup. The numerical results does maintain the characteristics of the scaling laws presented by Ahedo and Navarro Cavallé [20], in which there is a 'knee' that can be used as a desirable operating point, or a minimum value of the dimensionless parameter $\frac{\dot{m}R_{ion}L}{\pi R^2 m_i u_n C_s}$ that needs to be achieved to ensure efficient propellant use.

Moving on to the power efficiency η_P, an expression can immediately be obtained from equations 2.15 - 2.18.

$$\eta_P \equiv \frac{P_{exit}}{P} \approx \frac{1}{\left(1 + \frac{P_{backwall}}{P_{exit}}\right) + \frac{2\int_{-L}^{0} n_z(z,R)dz}{\beta n_0(0,0)R}}. \tag{3.9}$$

In the case where $T_e \gg 1$ i.e. $\eta_I \approx 1$ and maintaining the assumption for the magnetic nozzle performance, the value for $1 + \frac{P_{backwall}}{P_{exit}}$ is approximately 2.41 for xenon and 2.30 for argon, having a low dependence on propellant species. The factor for radial dissipation depends on the density profile within the source channel, however the density profile dependency is weak [24] and can be approximated as a constant. Therefore, it is possible to further approximate equation 3.9 into the form of

$$\eta_P \approx \frac{1}{\left(1 + \frac{P_{backwall}}{P_{exit}}\right) + \delta h_R \frac{L}{R}}, \tag{3.10}$$

where δ is a fitting parameter that can be used to identify the scaling law. Figure 3.2 shows a sample dataset with the fitting performed. Several trends are of interest. First, the scaling laws for classical and bohm diffusion differ due to the different scaling for h_R. The most notable difference is the scaling in relation to T_e. In the case of classical diffusion, a higher electron temperature improves confinement, leading to higher efficiencies. In addition, optimal confinement is easily achieved by moderate magnetic field strengths. However, when Bohm like collisions dominate, a higher electron temperature increases the

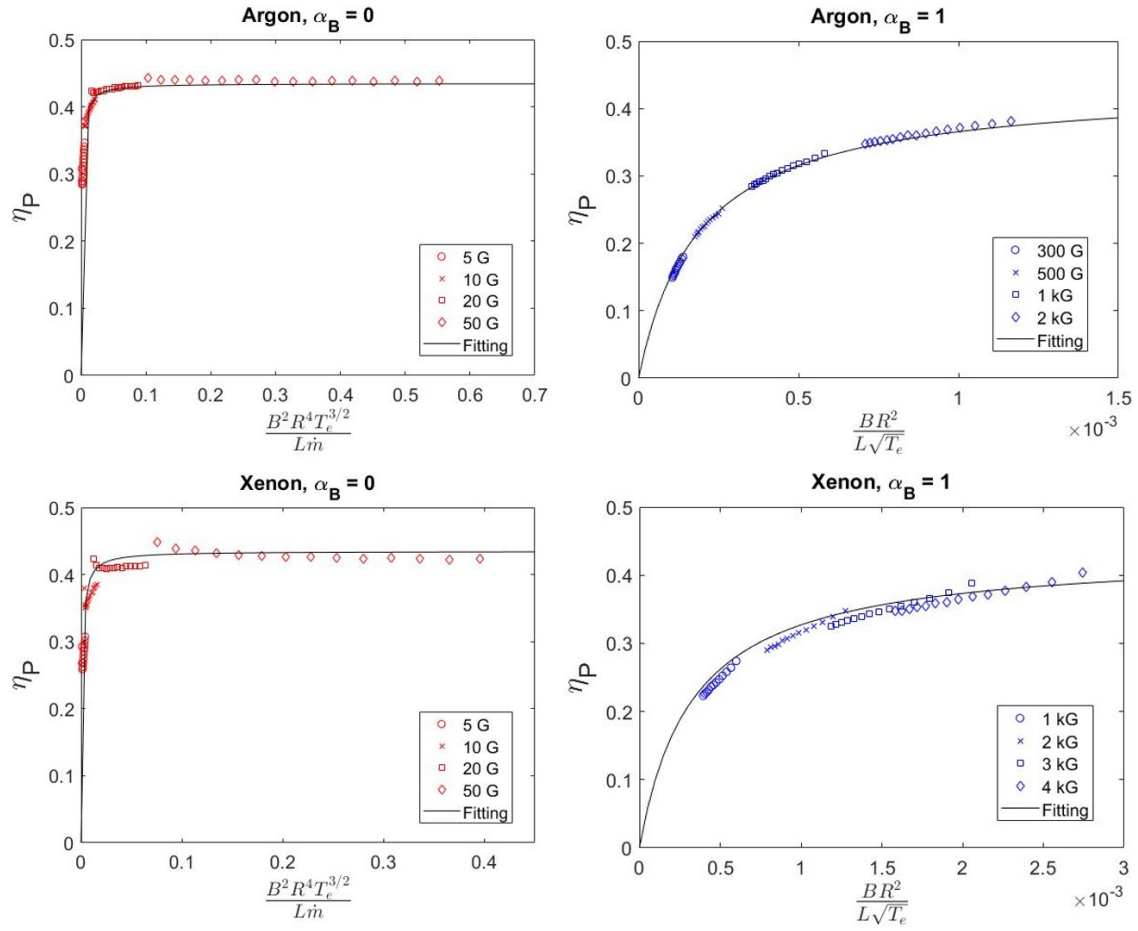

Figure 3.2: Power efficiency scaling with varied magnetic field and T_e. Other parameters are fixed at $R = 5cm$, $L = 10cm$, $\dot{m} = 1mg/s$.

diffusion rate and lowers the power efficiency. It is also difficult to achieve high confinement unless the magnetic field strength is increased over the typical range found in thrusters. In all cases, it can be seen that the scaling trends towards the asymptotic fit as the electron temperature becomes higher which is because of ionization losses. While lower electron temperatures appears like it yields a higher power efficiency, it is due to lower potential drops across the sheath and the decrease in propellant utilization rate is more prominent.

The ionization efficiency is plotted in figure 3.3, which shows the temperature dependent

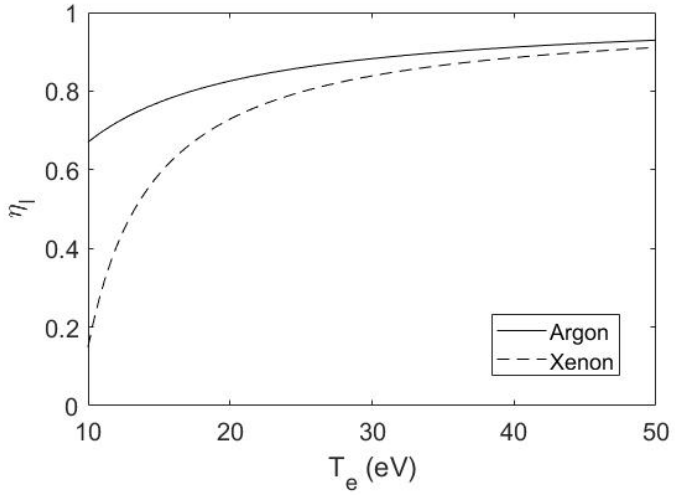

Figure 3.3: Ionization efficiency for argon and xenon assuming a perfect magnetic nozzle.

η_I described by equation 3.6. It can be seen that xenon generally yields a lower η_I, but approaches unity at moderately high electron temperatures. While the ionization energy of xenon is smaller than argon, the excitation energy and other collisional losses contribute to inefficiencies.

Now that all components of thrust efficiency have been discussed, it is possible to combine the asymptotic scaling laws into a general scaling law for thrust efficiency. The asymptotic thrust efficiency is a parameter of the five variables, R, L, $P(T_e)$, $\dot{m}$, and B. Figures 3.4 and 3.5 show the asymptotic scaling of thrust efficiency for argon and xenon respectively. The x axis value of $\frac{\dot{m}L}{R^2}$ represents the probability of ionization (η_d) and the y axis represents the confinement. It can be seen that the thrust efficiency generally scales with electron temperature, but the scaling of h_R may affect general scaling behavior. The inclusion of h_R in the y axis describes the effect of anomalous transport in a general case. In practice, h_R will be determined primarily through empirical means.

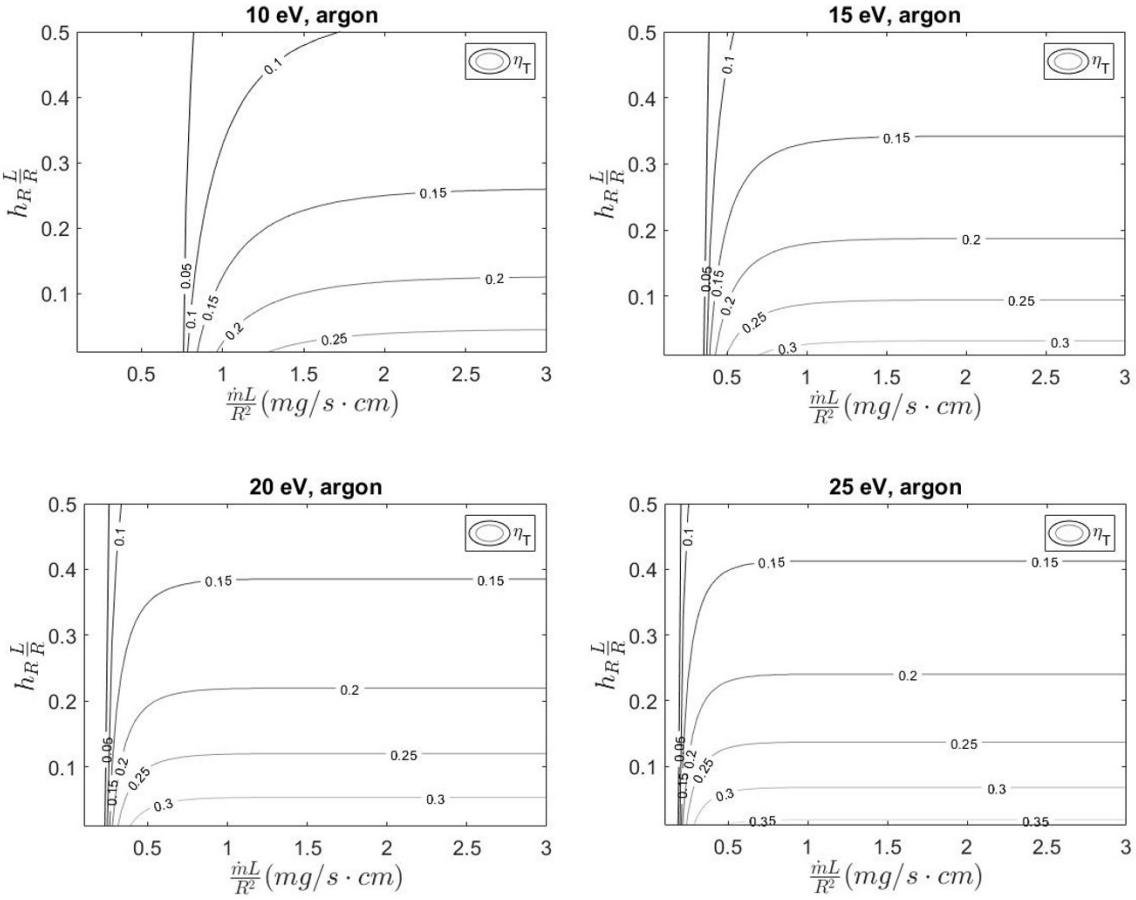

Figure 3.4: Asymptotic scaling of thrust efficiency for argon.

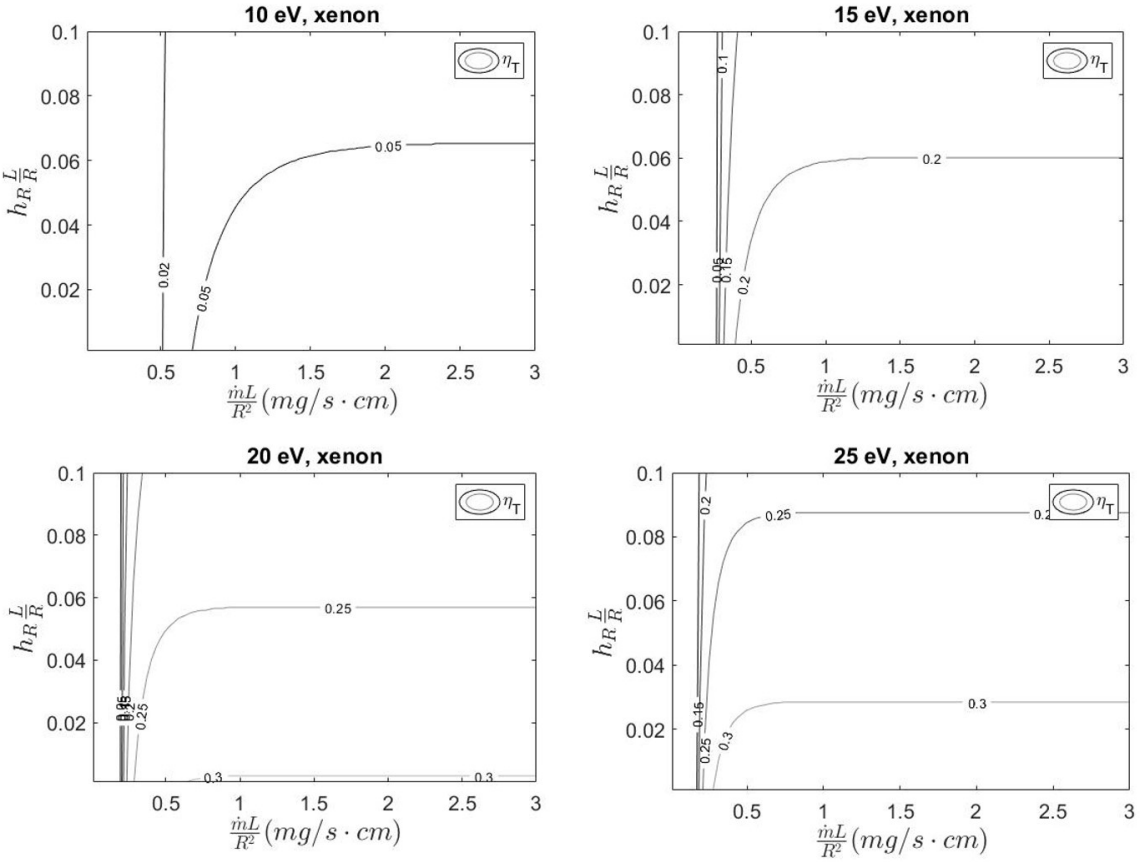

Figure 3.5: Asymptotic scaling of thrust efficiency for xenon.

3.0.2 Erosion scaling

The scaling of erosion characteristics are examined through the parameter I_W, which is defined in equation 1.3. In a general scaling perspective, traditional lifetime metrics in hours of operation are not intuitive, since the operational time of a thruster heavily depends on the specific operating conditions and structural design. I_W, which is the total impulse obtained per unit thickness of wall material eroded, is useful since it directly relates to the total delta-v obtainable throughout the thruster lifetime, and also allows comparison between different operating conditions.

The asymptotic scaling law for I_W can be derived from equation 1.3. The erosion rate can be expressed as

$$\nu_{er} = \Gamma_{wall} Y \frac{M_{wall}}{\rho_{wall}} = n_0 h_R C_s Y \frac{M_{wall}}{\rho_{wall}}, \tag{3.11}$$

where M_{wall} and ρ_{wall} are the atomic number and density of the wall material respectively. Since the first point of failure limits the thruster lifetime, the maximum value of ν_{er} within the channel is implied unless otherwise stated. From equation 2.21, $Y \propto \sqrt{T_e} - \delta_Y$, where $\delta_Y \approx 2.15$ for argon and $\delta_Y \approx 2.04$ for xenon. While the equation suggests that δ_Y can be ignored when the electron temperature is large, it remains significant in the typical electron temperature ranges. Adopting equation 3.1 for thrust and the scaling for h_R, it is possible to arrive at the conclusion that

$$I_W \propto \frac{B^2 R^5 T_e^2}{\dot{m}(\sqrt{T_e} - \delta_Y)}, \qquad (Classical) \tag{3.12}$$

$$I_W \propto \frac{B R^3}{\sqrt{T_e} - \delta_Y}. \qquad (Bohm) \tag{3.13}$$

The most notable difference in the two dominant diffusion mechanism is the dependence on T_e, where if classical diffusion is dominant, it is beneficial to operate in a high temperature, and if Bohm-like diffusion is dominant, a higher electron temperature results in a

poorer erosion characteristic. This presents a unique trade-off, as higher temperatures are generally desired for higher efficiencies. The scaling laws can be observed from the numerical results. Figures 3.6 - 3.9 shows the scaling of I_W for argon and xenon, in the case of purely classical diffusion and including the full effects of anomalous Bohm-like transport. The scaling laws are verified by collapsing the data onto the form presented by equations 3.12 and 3.13. The deviation in lower electron temperatures are not of significance, since it is in a regime where the neutral component of the thrust becomes significant due to low ionization rates and plume velocities. Another notable difference is the difference in values for the case of classical diffusion and Bohm diffusion, which results from the difference in confinement.

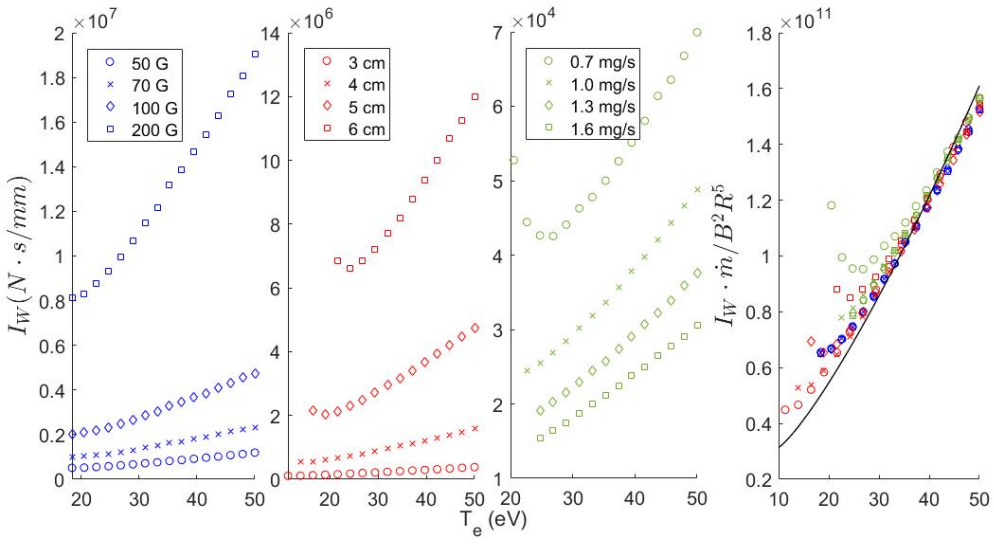

Figure 3.6: I_W scaling of argon in the case of purely classical diffusion. Parameters are $B = 1kG$, $R = 5cm$, $L = 10cm$, $\dot{m} = 1mg/s$ unless specified.

Figures 3.10 and 3.11 show the effect of different contributions of Bohm diffusion against the asymptotic scaling of I_W for argon and xenon. It can be seen that even a small amount of Bohm-like diffusion drives the scaling law, but the amount of contribution greatly affects the predicted value of I_W. Table 3.2 lists some data for commercial Hall thrusters for

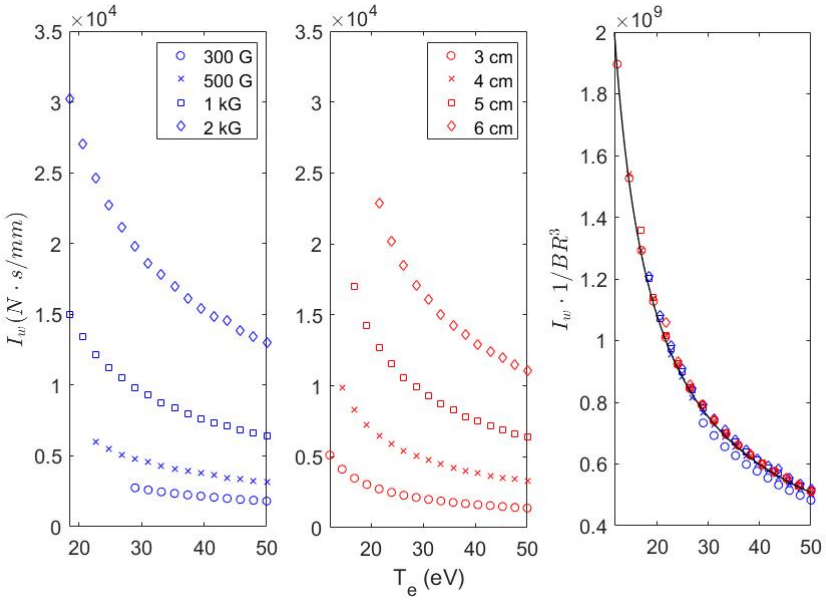

Figure 3.7: I_W scaling of argon in the case of full Bohm-like diffusion. Parameters are $B = 1kG$, $R = 5cm$, $L = 10cm$, $\dot{m} = 1mg/s$ unless specified.

comparison. The parameters are calculated from reported values of thrust and erosion rates found in literature, and may vary depending on the specific operating conditions of the thrusters. Comparing these values to figure 3.11, it can be seen that the lifetime performance of electrodeless thrusters can be comparable to Hall thrusters in the case of strongly dominant Bohm-like diffusion. The results show that there is potential for electrodeless thrusters with a magnetic nozzle to overcome the lifetime limitations of Hall thrusters, but the claim that they are free from such limitations is debatable.

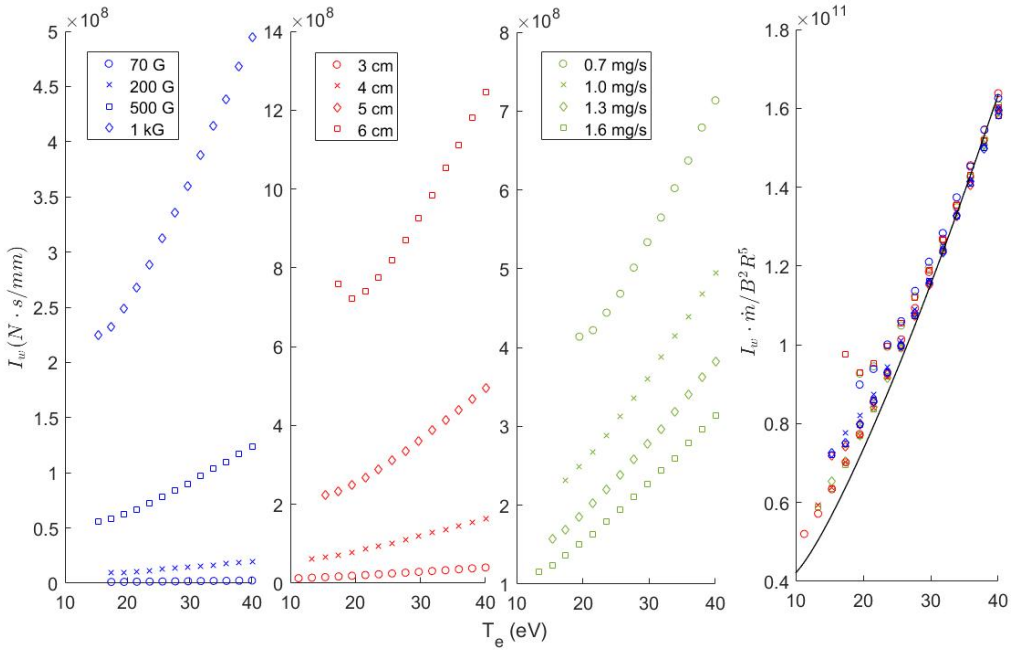

Figure 3.8: I_W scaling of xenon in the case of purely classical diffusion. Parameters are $B = 1kG$, $R = 5cm$, $L = 10cm$, $\dot{m} = 1mg/s$ unless specified.

Thruster	$I_W(kN \cdot s/mm)$	$I_{sp}(s)$
SPT-100[53][54]	30	1570
SPT-70[55][56]	40	-
BHT-600[57]	40	1500

Table 3.2: Calculated values of I_W and reported specific impulses of several commercial Hall thrusters.

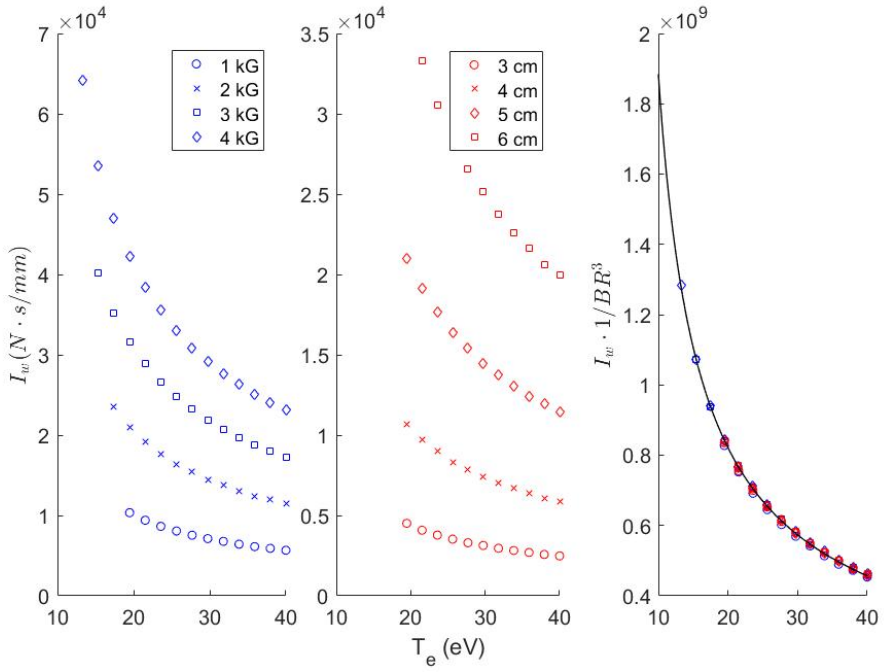

Figure 3.9: I_W scaling of xenon in the case of full Bohm-like diffusion. Parameters are $B = 1kG$, $R = 5cm$, $L = 10cm$, $\dot{m} = 1mg/s$ unless specified.

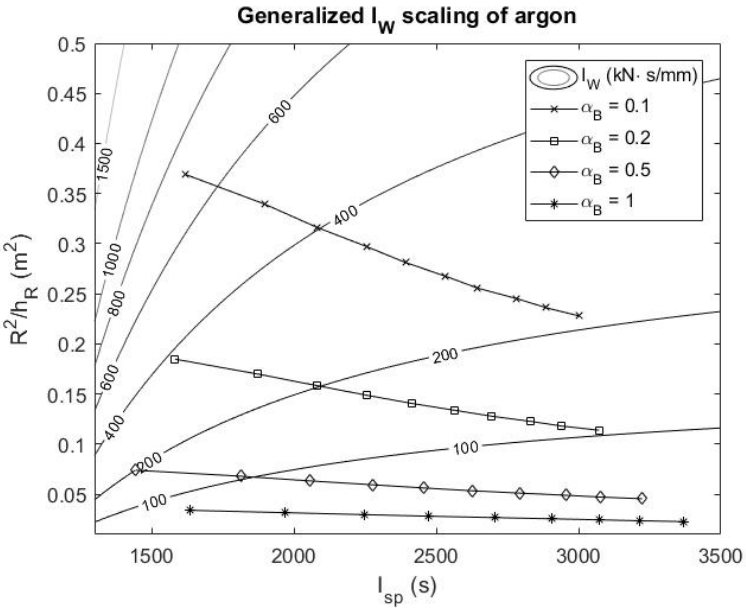

Figure 3.10: I_W scaling of argon and sample trends with varying α_B. Parameters are $B = 500G$, $R = 5cm$, $L = 10cm$, $\dot{m} = 1mg/s$.

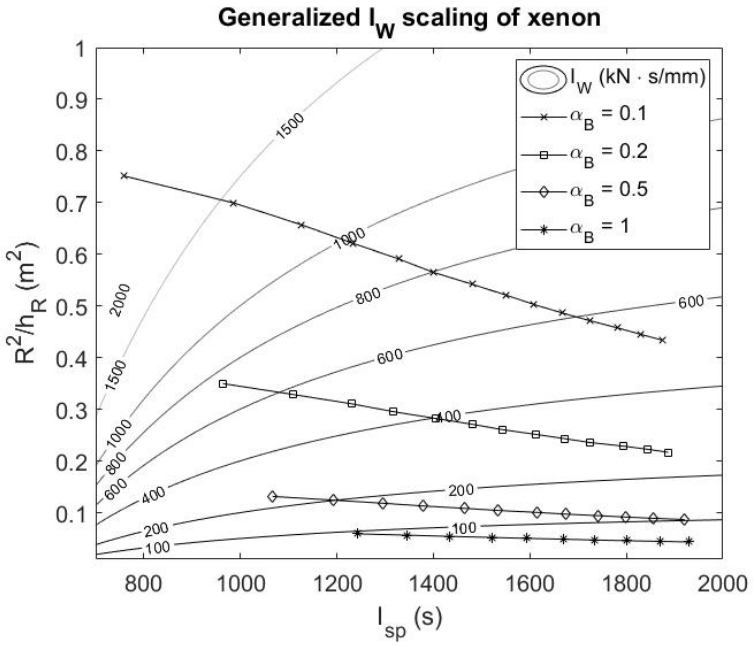

Figure 3.11: I_W scaling of xenon and sample trends with varying α_B. Parameters are $B = 2kG$, $R = 5cm$, $L = 10cm$, $\dot{m} = 1mg/s$.

Chapter 4

EXPERIMENTAL DATA

While experimental data on wall erosion could not be obtained for the duration of this study, supplementary data using an ECR thruster in the University of Washington SPACE Lab were used to compare empirical scaling data to the predicted scaling laws. This also provides information on the validity of the scaling laws to ECR thrusters.

4.1 ECR Thruster

The thruster that was used in the tests is the SPACE Lab Alternative Propellant ECR eXperimental (APEX) thruster, which operates on 2.45 GHz microwave input. The channel diameter is 0.875 inches, the channel depth is 0.9 inches, and has a 1/8 inch diameter copper rod for the center antenna. The channel is machined out of Macor ceramic to resist corrosion due to alternative propellants such as water, however all the data presented here is operated on argon. Figure 4.1 shows the SPACE Lab APEX thruster viewed from the front. The APEX thruster uses six permanent ring neodymium magnets to generate a diverging magnetic field with a maximum axial field strength of approximately 1 kG. The resonance region occurs around 875 G for a 2.45 GHz source. The axial field profile is shown in figure 4.2. The APEX thruster is operated in the SPACE test facility, which has a background pressure of $2 \times 10^{-7} torr$ and pumping speed of 12 kL/s xenon and 60 kL/s H2O.

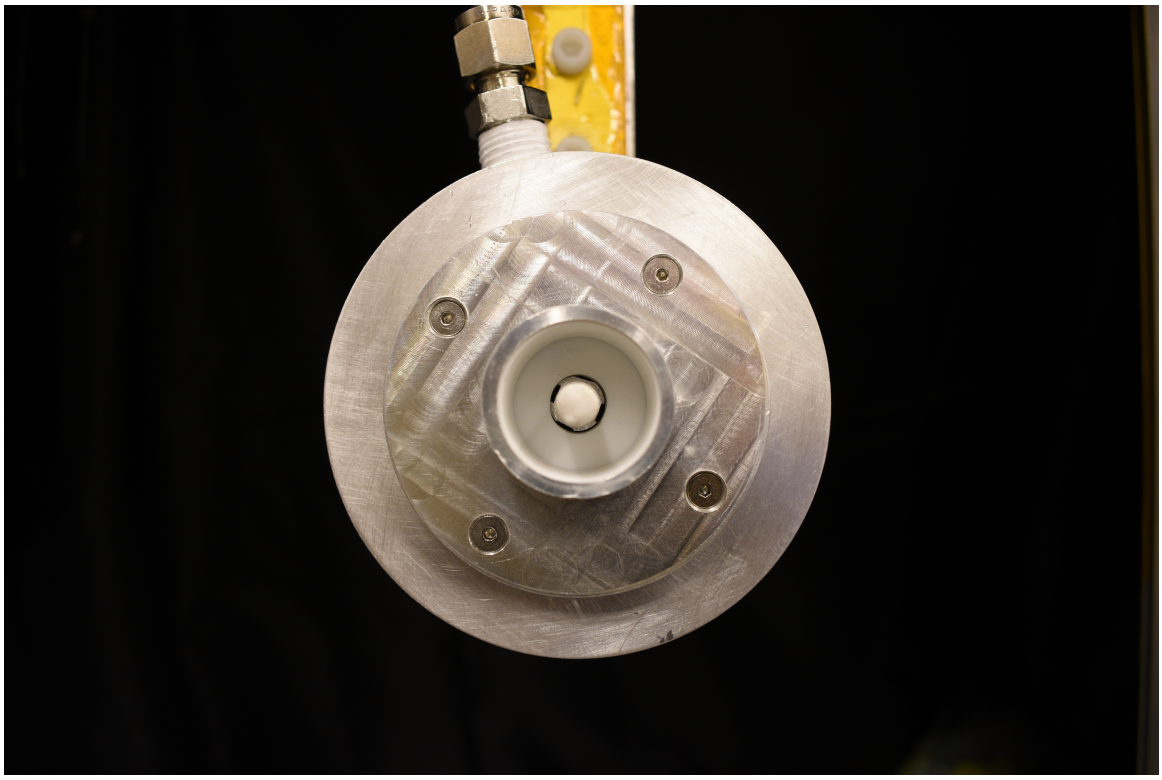

Figure 4.1: The SPACE Lab APEX thruster viewed from the front. Here, a 1/4 inch diameter alumina sleeve is inserted around the center antenna. The propellant in injected axially through the channels around the antenna.

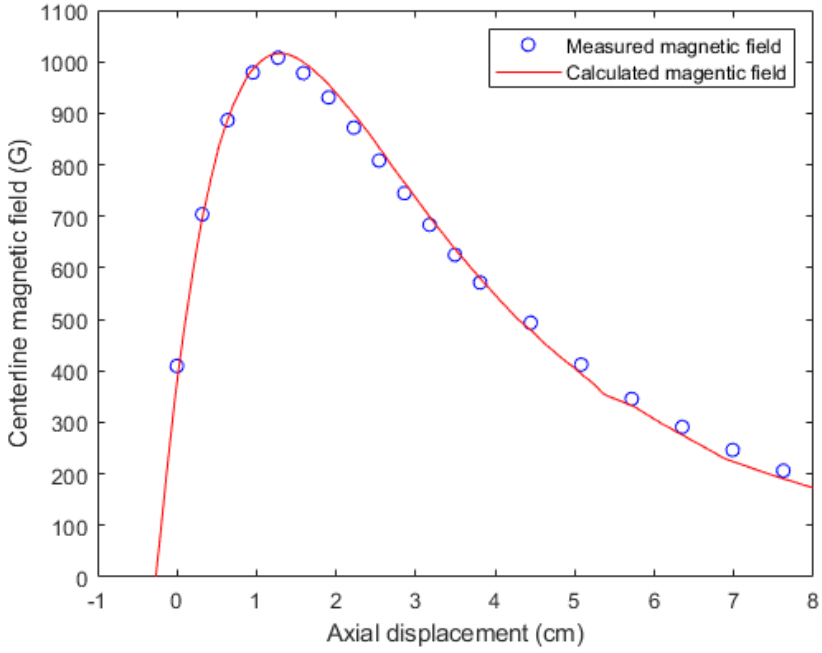

Figure 4.2: The axial magnetic field profile of the APEX thruster.

4.2 Diagnostics

4.2.1 $E \times B$ Probe

An E×B probe, or Wein filter, was made to analyze the plume of the ECR thruster. The probe operates by passing the test particles, or plume ions, through a perpendicular magnetic field and electric field. The particle travels straight only when the Lorentz force is zero, or when $v = E/B$, where v is the velocity of the particle. Therefore, it is possible to selectively detect particles with a certain velocity by varying the electric field strength. Figure 4.3 shows the operating principle of the EXB probe. The probe body was constructed out of 3/8 inches thick carbon steel to contain the magnetic field within the probe [58]. The bias plates were made of 4×1.5 in aluminium plates, and had a separation of 1.5 inches. The bias voltage was applied through a Kepco 500M bipolar operating supply. Nylon bolts and

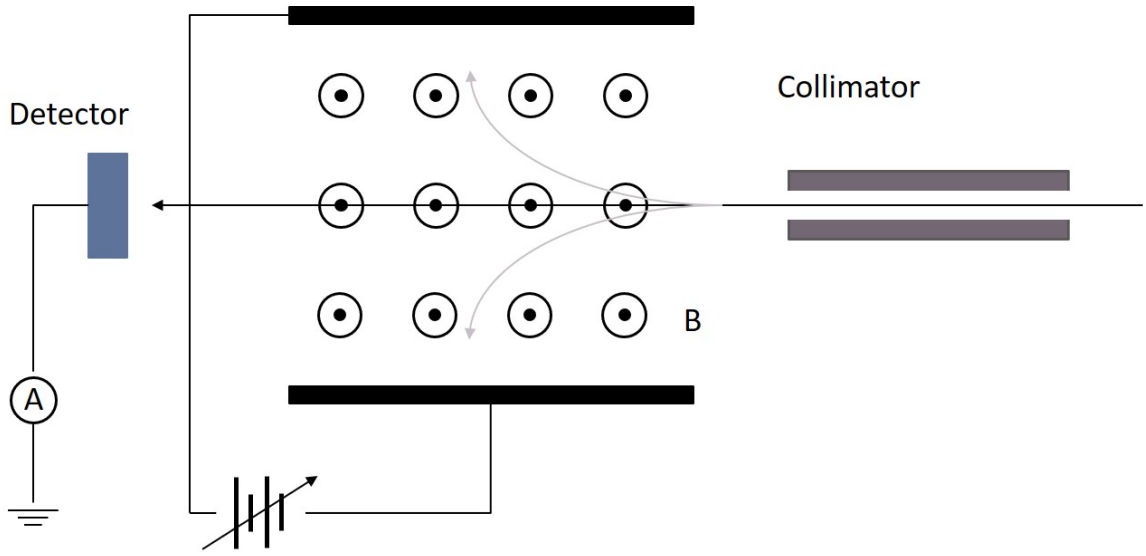

Figure 4.3: Schematic of EXB probe operation

garolite spacers were used to isolate the plates from the body. Permanent ceramic magnets were used to generate the magnetic field within the test section, and was measured to be within the range of $0.110 - 0.129T$. The collimator was 2.5 inches in length and had a orifice diameter of 0.069 inches. It was constructed using telescoped stainless steel tubes and was attached to the probe through a threaded Yor-Lok fitting for easy replacement. The detector was a tungsten electrode carved to minimize the effect of secondary electron emissions [59], and was isolated from the probe body through PTFE tubing. The output was detected via a Keithley 6485 PicoAmmeter. The detector electrode was originally constructed out of graphite, but was replaced with tungsten due to poor sensitivity. All electrical connections are achieved by BNC coaxial cables to shield the signal from the ambient plasma and microwave noise, and the probe body was grounded through the coaxial cable of the detector. Figures 4.4 and 4.5 shows the constructed EXB probe and its installation.

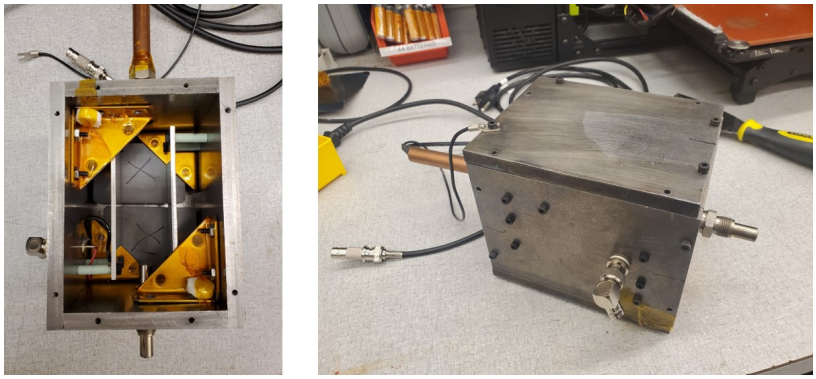

Figure 4.4: Top-down interior view of the EXB probe (left) and exterior view of the EXB probe (right). The probe is symmetric in geometry and the topside magnets are removed for visibility in the picture.

4.2.2 Langmuir probe

Since the EXB probe only provides relative information, a Langmuir probe (LP) is used to obtain the electron temperature and plasma density. The LP was constructed using a tungsten electrode and had a diameter of 1 mm and length of 5 mm. The circuit of a LP can be seen in figure 4.6. The Langmuir probe operates by measuring the current collected through the electrode submerged in the plasma over a swept voltage. A Kepco 500M bipolar operating supply was used to sweep the voltage, and a 1 kOhm resistor was used to measure the current.

For a Maxwellian electron distribution, the collected current can be related to the bias voltage by

$$ln|I - I_{sat}| = (V - V_f)/T_e + constant, \tag{4.1}$$

where I_{sat} is the ion saturation current and V_f is the plasma floating potential. Therefore by taking the logarithm of the collected current and calculating the slope, it is possible to obtain the electron temperature. The ion saturation is the collected current when the signal saturates in the negative limit of the bias voltage. The plasma density is then obtainable

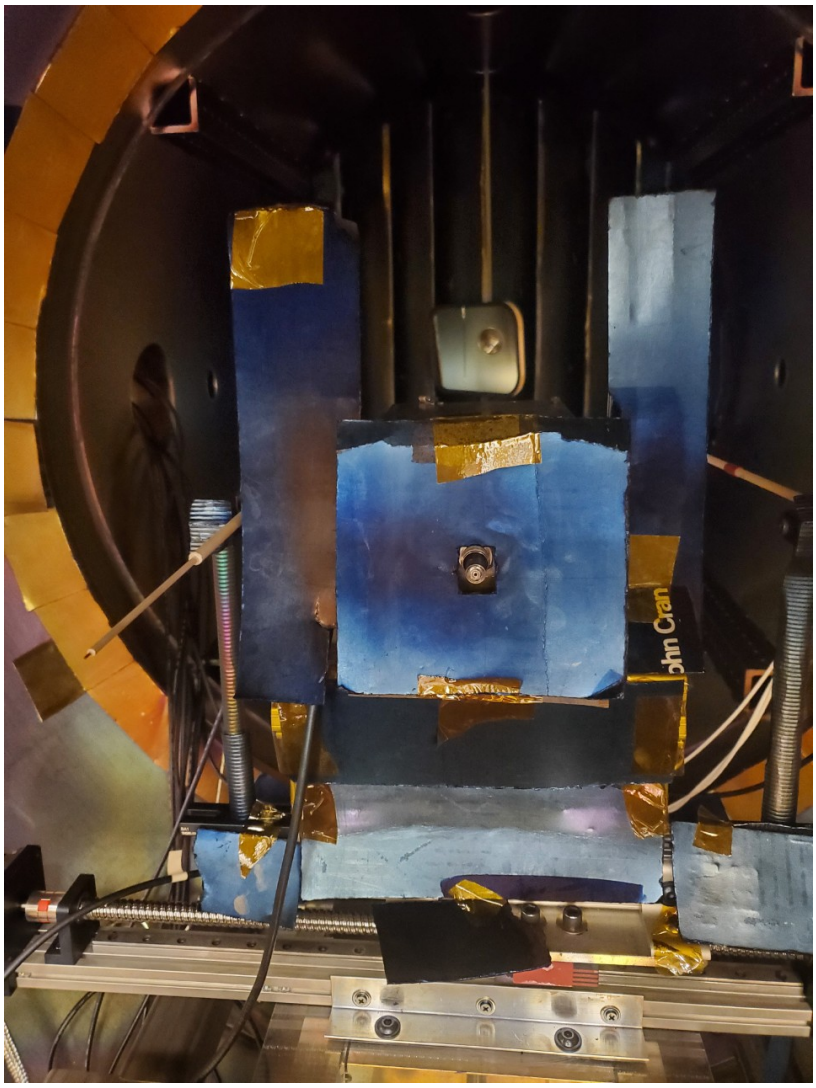

Figure 4.5: Picture of EXB probe and Langmuir Probe installed in the SPACE test facility. The probe surface and supporting structures are covered in graphite sheets to prevent sputtering.

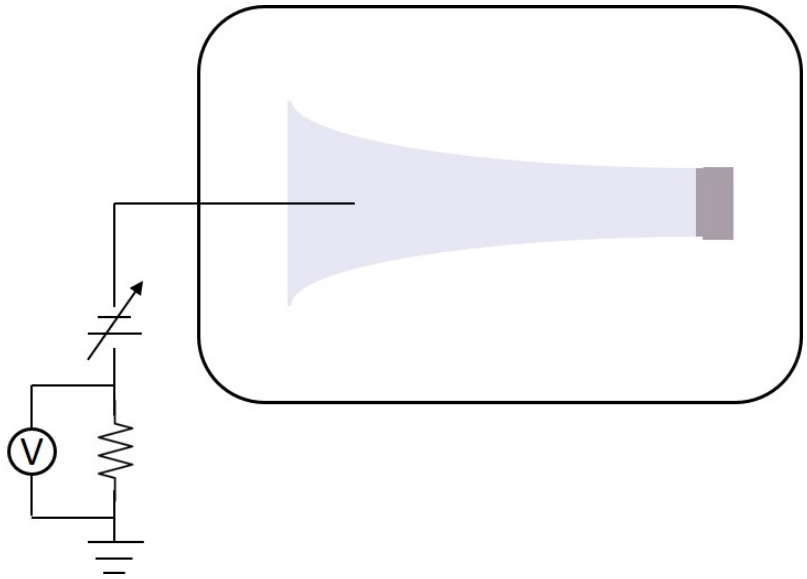

Figure 4.6: Schematic of Langmuir probe measurement.

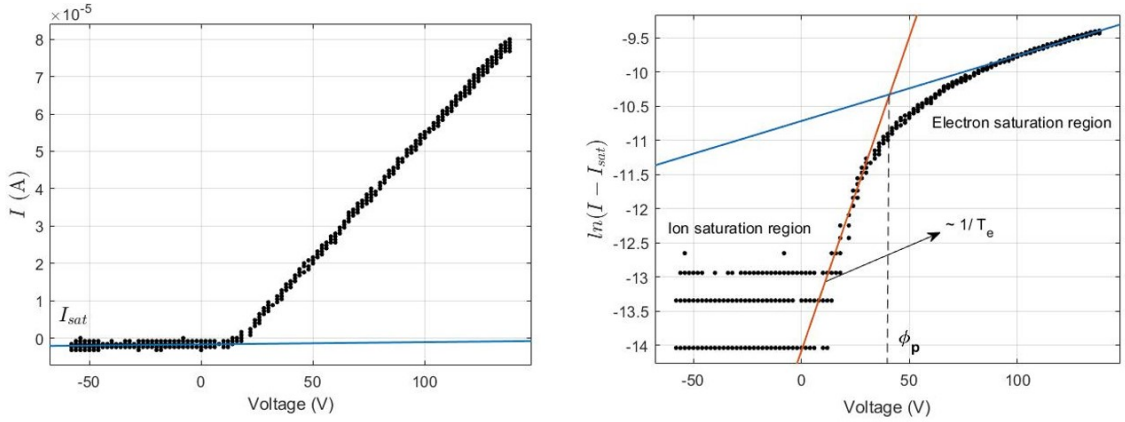

Figure 4.7: Example of Langmuir probe trace and analysis. The trace is taken at 3sccm argon, 30W power, and 12 inches from the thruster exit plane.

through the relation

$$I_{sat} = A_p exp\left(-\frac{1}{2}\right) en\sqrt{\frac{eT_e}{m_i}}, \tag{4.2}$$

where A_p is the area of the probe, which is approximated as the side areas in a cylindrical probe. Figure 4.7 illustrates how a LP trace is analyzed.

4.3 Results

EXB probe and LP traces were taken over a range of input powers and mass flow rates. Measurements were taken at a distance of 12 inches from the thruster exit plane to the collimator entrance and LP, and along the axis of the thruster. Measurements closer to the exit plane were infeasible due to the magnetic attraction between the thruster and the EXB probe.

Figures 4.8 and 4.9 show the EXB probe traces for various input powers and mass flow rates, respectively. Various methods of analyzing the probe trace can be found in literature [60]. Hofer [61] suggested the use of peak heights, which is the most simple and straightforward method provided that the variation in peak widths can be neglected. Beal [62] suggested triangle fitting, which is a simple method to account for peak broadening. The area of the triangle is then proportional to the peak height and half-width at half-peak. Linnell [63] suggested a method of fitting the data to a Gaussian profile to capture the peak characteristics more accurately. Another approach to curve fitting was proposed by Kim [58], which argued that the curve would be somewhere between a Gaussian function due to collisional processes, and a Druyvesteyn profile due to a steady state distribution in a steady electric field with elastic collisions. In this work, the approach by Linnell was adopted, due to the fact that the peak is not clearly identified from the raw signal and the peak width is significant. The fit and position of the peak is shown along with the data in figures 4.8 and 4.9. Having identified the position of the peak, it is possible to estimate the ion velocity by

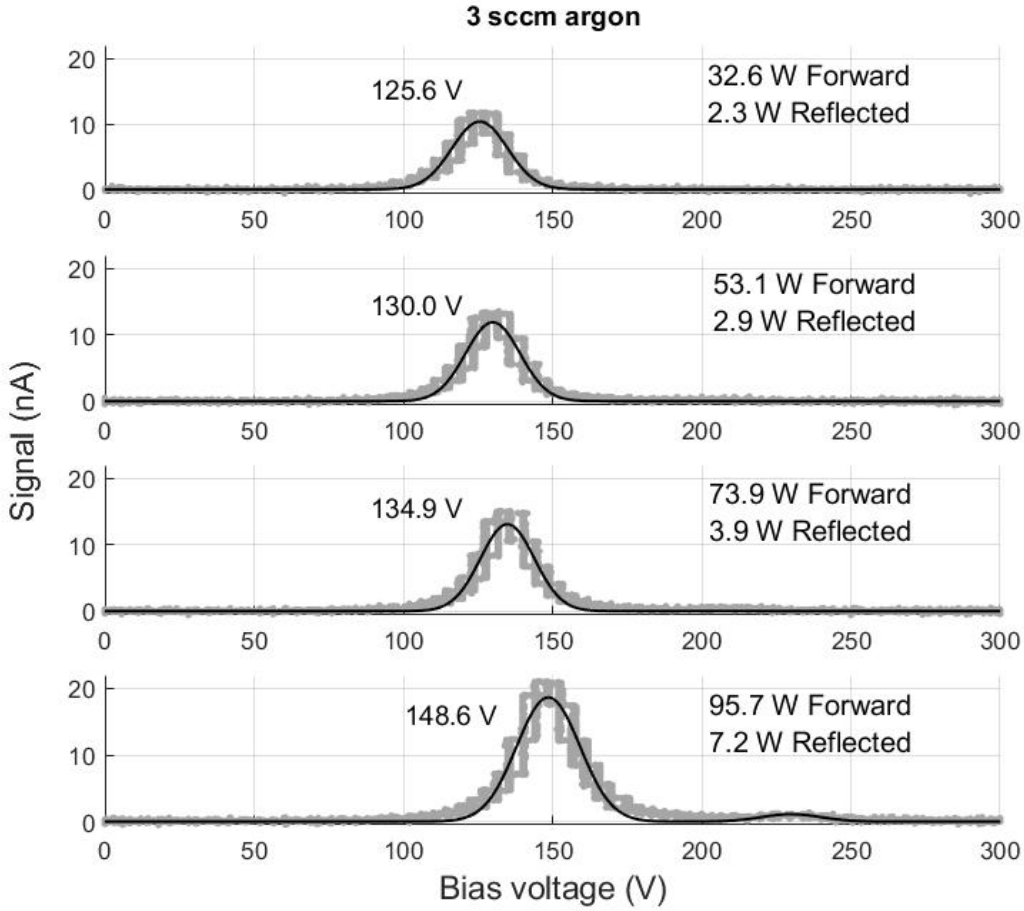

Figure 4.8: EXB probe traces over varied input power. Doubly charged ions can be seen in the highest input powers.

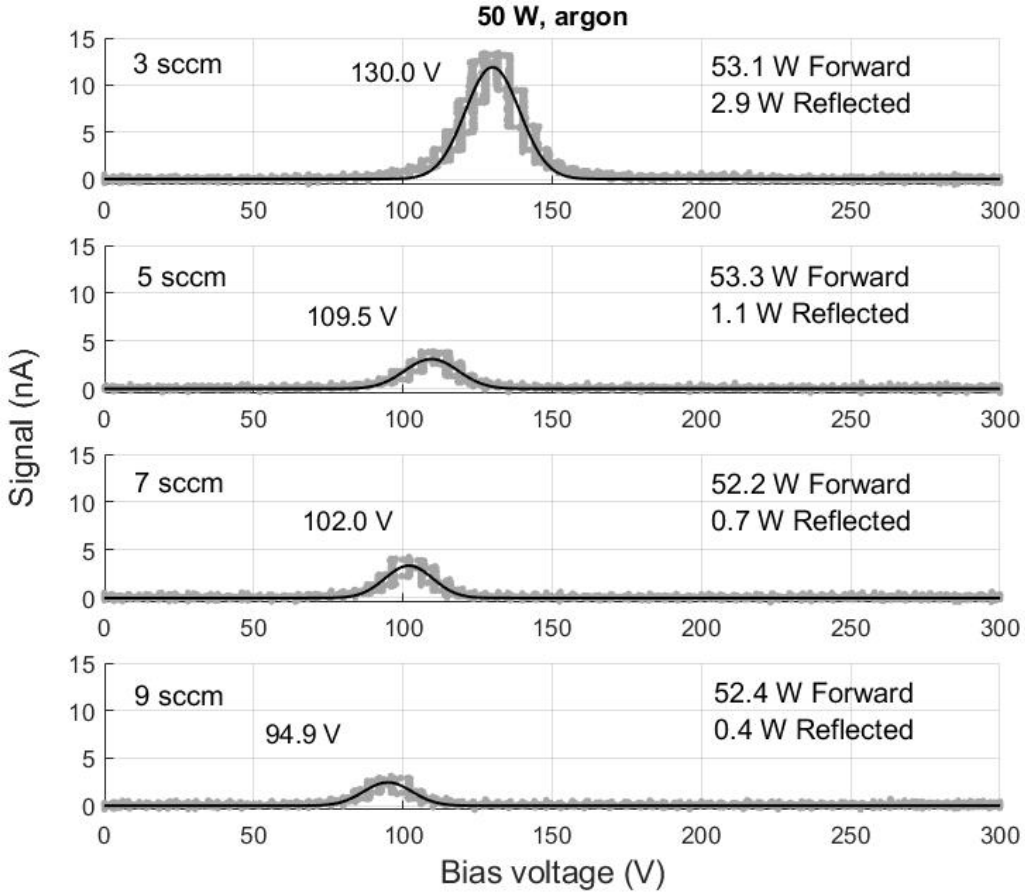

Figure 4.9: EXB probe traces over varied mass flow rate.

the relation

$$v_{ion} = \frac{E}{B} = \frac{V_{bias}}{dB}, \tag{4.3}$$

where V_{bias} is the bias voltage of the probe and $d = 0.0381m$ is the distance between the bias plates.

Figure 4.10 shows the electron temperature and density calculated from the LP traces. As input power increases, the electron temperature rises as expected. The plasma density also increases as higher propellant utilization rates are achieved, which flattens out as it approaches unity. It should be noted that there are two effects competing against each other, which is the increased density due to more ionization leading to higher propellant utilization rates, and a density decrease caused by a higher exhaust velocity. Therefore, as higher input powers are reached, the measured plasma density will eventually decrease. This is not seen in the ranges of this experiment, and should be considered together with the electron temperature and plasma velocity to assess performance characteristics. For increased propellant mass flow rate, it can be seen that the electron temperature decreases, as ionization losses and wall losses become more prominent. On the other hand, the plasma density is seen to increase. Similarly to the previous case of varied power, the effect of lower propellant utilization rates due to lower electron temperatures act to lower the plasma density, but having more propellant creates additional plasma that causes an increase in plasma density.

Having obtained the electron temperature and density data, it is possible to relate it back to the EXB probe trace. Figure 4.11 shows the estimated plume velocity to the electron temperature obtained by the LP data calculated through equations 4.1 and 4.2. The data corresponds to those shown in figures 4.8 and 4.9. It should be noted that the error shown in the plot is not random, and is from the upper and lower limits of the magnetic field strength measured in the test section. Since the magnetic field is constant for all tests, the

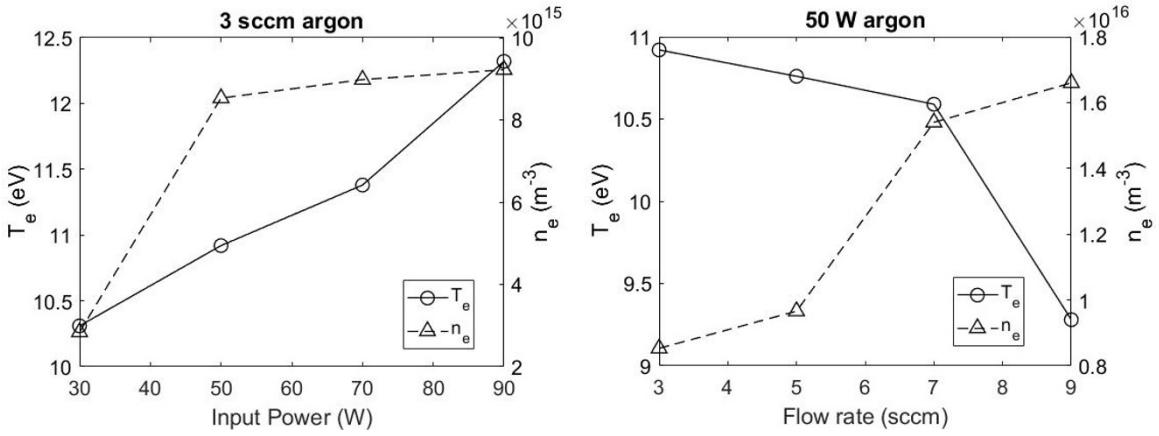

Figure 4.10: Electron temperature and density data calculated from Langmuir probe trace.

trend is valid and all data will shift in a consistent manner. While the ion velocity in the plume increases with electron temperature as expected, a sharper decline is observed when the mass flow rate is increased. It can be speculated that this is due to the presence of more neutrals in the plume and vacuum facility slowing down the ions due to collisional processes, however further testing and investigation into facility effects is required for validation.

The height of the peak, or specifically the area under the Gaussian fit, is also of interest. Ideally, the area of the fit will be proportional to the flux of incident ions, which is the plume ion velocity times the plasma density at the collimator entrance. This relation can be written as

$$I_{exb} = eZ_i n_i u_i A_c, \tag{4.4}$$

where I_{exb} is the collected current, Z_i is the charge state of the ion, n_i and u_i are the ion density and velocity, and A_c is the area of the collector or collimator orifice, whichever is smaller. Figure 4.12 shows the area of the fit divided by the measured plasma density against the estimated plasma velocity. This demonstrates that apart from a single outlier case, the results agree well with the form stated by equation 4.4.

Figure 4.13 shows the measured electron temperature and the results from the numerical

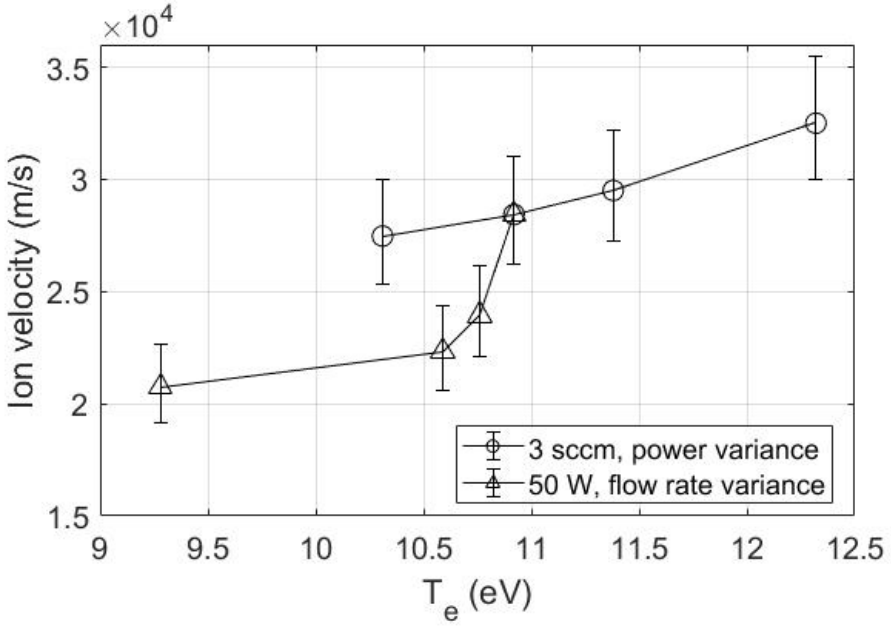

Figure 4.11: Measured plume velocity against measured electron temperature.

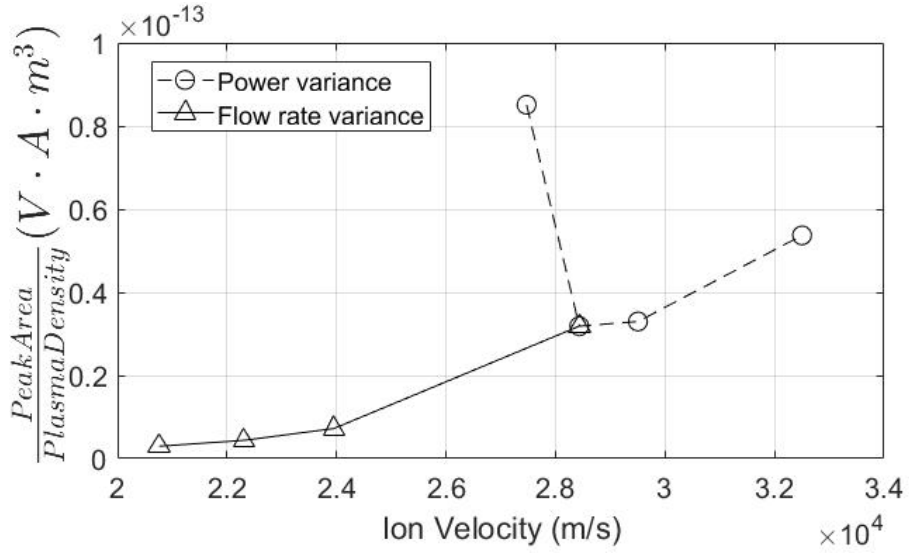

Figure 4.12: EXB probe trace peak area divided by measured plasma density against estimated plasma velocity.

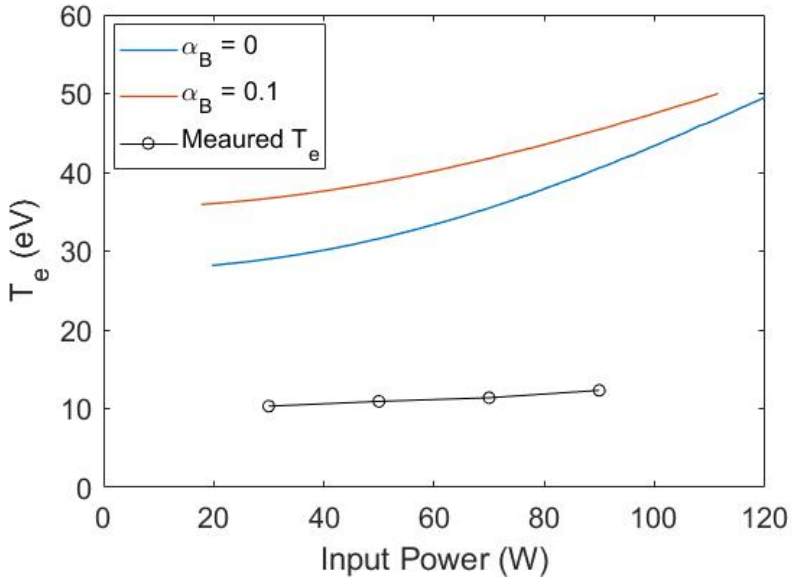

Figure 4.13: Measured electron temperature of thruster compared to the numerical results of the model. The parameters used for the geometry are $B = 875G$, $R = 1.1cm$, $L = 2.3cm$.

model presented. The parameters used are the thruster channel radius, depth, and resonance magnetic field outlined in section 4.1. It can be seen that while the scaling law appears to be consistent, the predicted values of electron temperature differs significantly. However this does not necessarily invalidate the model as this can be attributed to a variety of factors. The largest difference between the APEX thruster and the model is the geometry and method of energy coupling. The center antenna reduces the area in the channel, effectively reducing the radius of the thruster. In addition, it creates a secondary wall for the plasma to diffuse into, changing the radial density profile and increasing wall losses. The energy coupling is also highly localized in the resonance layer and around the center antenna, which also leads to localized differences in electron temperature. This has been predicted by Sánchez-Villar *et. al.* through PIC simulations, and can also be visually confirmed through the plume as shown in figure 4.14. It is also important to note that the measurements were not made at the exit plane and further down the plume, which accounts for the cooling of the electrons.

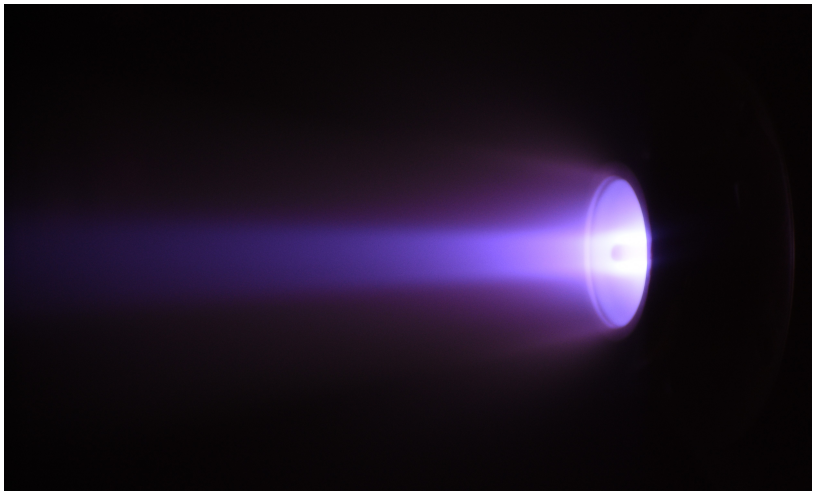

Figure 4.14: Picture of the plume from the APEX thruster. The focused plume around the center antenna is visible.

Overall, these characteristics can account for the difference in model and measured results, and suggests different modeling methods should be used for ECR thrusters.

Chapter 5

CONCLUSION

Despite the increased interest in electrodeless plasma thrusters, there has been no work yet studying the lifetime characteristics of such thrusters in detail. While experimental data is much desired, it is also necessary to model the erosion characteristics to predict scaling laws and identify any trade offs that may affect the design of a thruster. In this thesis, asymptotic scaling laws for erosion and performance metrics are derived through simplified balance equations, and a self-closed numerical model is formed to evaluate the validity of the derived scaling laws. The physical model starts off by adopting a quasi 1-D two species approach found in literature by Ahedo [20][27] and Lafleur[24] to obtain the electron temperature, plasma density, and wall flux within a plasma source channel. Then simplified sheath scaling laws and semi-empirical sputtering models were used to estimate the wall erosion rate. Through the derivation of thrust and erosion rates, wall impulse, which is the amount of impulse obtained per unit thickness of wall material eroded, was used to evaluate the erosion characteristics across various operating parameters. In addition, this thesis contains the design of an EXB probe for thruster plume diagnostics and test results on a ECR thruster.

5.0.1 Erosion and Performance Scaling Laws

The scaling laws for an electrodeless plasma thruster were broken down into propellant utilization rate, power efficiency, and ionization efficiency. In the case of propellant utilization rate, the scaling was obtained as a function of $\frac{\dot{m}R_{ion}L}{\pi R^2 m_i u_n C_s}$, which is the probability of a particle becoming ionized before leaving the channel. It was shown that this parameter must

be above a threshold value to obtain high utilization rates. In addition, effects of anomalous transport was shown to negatively impact the scaling, and made it require higher magnetic field strengths to approach asymptotic scaling laws. In the case of power efficiency, which is the ratio between the amount of power directed out the plasma exit and total input power, the scaling laws depended on the dominant diffusion mechanism. Most noticeably, a higher electron temperature was desired in the case when classical diffusion dominates, but a higher electron temperature led to lower efficiencies in the case of dominant Bohm-like diffusion. Similar to propellant utilization rates, the presence of anomalous transport significantly affected the required magnetic field strengths for high efficiencies. Ionization efficiencies are unaffected by diffusion mechanisms, and motivates operation in higher electron temperatures, or higher input powers. The individual scaling laws were combined to obtain scaling laws for thrust efficiency. The asymptotic scaling laws for wall impulse were also derived from the physical model. It was shown that the scaling laws heavily depend on the dominant diffusion mechanism, as wall flux directly drives the erosion rate. When classical diffusion dominates, $I_W \propto \frac{B^2 R^5 T_e^2}{\dot{m}(\sqrt{T_e}-\delta_Y)}$ whereas when Bohm-like diffusion dominates $I_W \propto \frac{BR^3}{\sqrt{T_e}-\delta_Y}$. This result highlights an important trade-off in the presence of Bohm-like diffusion since thrust efficiency generally benefits from higher electron temperatures, but this negatively impacts lifetime characteristics. This suggests that the diffusion mechanism must be well characterized when designing a thruster, and motivates further experimental and theoretical work on erosion mechanisms. Comparison of estimated ranges of wall impulse to those of existing Hall thrusters predict that the lifetime expectancy of electrodeless plasma thrusters can be comparable to those of Hall thrusters, motivating further examination of the claim that electrodeless plasma thrusters are not subject to lifetime limitations.

5.0.2 EXB probe design and diagnostics

As part of this thesis, an EXB probe was designed and used as a diagnostic for the plume of the SPACE Lab APEX ECR thruster. The probe successfully measured the plume velocity and was able to distinguish doubly charged ions at higher operating powers. A Langmuir probe was used to measure the electron temperature and plasma density. Electron temperature increased with input power, and decreased with increased mass flow rates as expected. The estimated plume ion velocity increased with electron temperature as expected, but exhibited a overall downwards shift in larger mass flow rates. This is speculated to be due to increased neutral density and collisional effects, but could not be confirmed through the collected data. Correlation between the plasma flux and the collected current was mostly linear, confirming that the EXB probe was operating as expected.

5.0.3 Future work

While the work in this thesis provides an overview of erosion scaling in electrodeless plasma thrusters, it lacks the experimental results to confirm the results. Therefore direct measurements of wall erosion rates in various operating conditions is essential to both confirming the validity of the model and finding any discrepancies. The use of quartz microbalance (QCM) sensors and profilometers are both possible ways to measure the erosion rate of thrusters, similar to those used in Hall thruster erosion measurements. Such data are not yet existent in literature, and would be valuable for pushing electrodeless thruster concepts into practical use. In this research, it has been established that the scaling laws heavily depend on the dominant diffusion mechanism. In literature, both classical diffusion and Bohm diffusion are reported in helicon plasma sources, which motivates further understanding of plasma diffusion in order to accurately estimate lifetime characteristics as well as other performance metrics. Furthermore, the power coupling mechanism of the plasma is also a poorly understood area and should be investigated.

The EXB probe can be further used for plume diagnostics. Measurements along the axis as well as at an angle from the centerline can provide spacial velocity and composition data for the plasma plume. Several improvements can be made to the EXB probe, which mostly involves reducing the collimator diameter to improve resolution while maintaining a good signal-to-noise ratio. Such diagnostics can be used to analyze charge exchange collisions in plasma plumes, as well as identifying facility effects.

BIBLIOGRAPHY

[1] Robert G Jahn. *Physics of electric propulsion*. Courier Corporation, 2006.

[2] SN Bathgate, MMM Bilek, and DR Mckenzie. Electrodeless plasma thrusters for spacecraft: a review. *Plasma Science and Technology*, 19(8):083001, 2017.

[3] Benjamin Wachs and Benjamin Jorns. Background pressure effects on ion dynamics in a low-power magnetic nozzle thruster. *Plasma Sources Science and Technology*, 29(4):045002, 2020.

[4] JP Sheehan, Benjamin W Longmier, Ingrid Reese, and Timothy Collard. New low-power plasma thruster for nanosatellites. In *50th AIAA/ASME/SAE/ASEE Joint Propulsion Conference*, page 3914, 2014.

[5] Timothy Ziemba, John Carscadden, John Slough, James Prager, and Robert Winglee. High power helicon thruster. In *41st AIAA/ASME/SAE/ASEE Joint Propulsion Conference & Exhibit*, page 4119, 2005.

[6] Justin M. Little. *Performance scaling of magnetic nozzles for electric propulsion*. PhD thesis, Princeton University, January 2015.

[7] Anna J Sheppard and Justin M Little. Scaling laws for electrodeless plasma propulsion with water vapor propellant. *Plasma Sources Science and Technology*, 29(4):045007, mar 2020.

[8] D Staab, A Frey, A Garbayo, L Shadbolt, Andrea Lucca Fabris, Antonio Gurciullo, Pascaline Grondein, Rachel Moloney, D Faircloth, and S Lawrie. Aquajet: an electrodeless ecr water thruster. In *Space Propulsion Conference Proceedings 2018*, 2018.

[9] F. R. Chang Dıaz. An overview of the vasimr engine: High power space propulsion with rf plasma generation and heating. *AIP Conference Proceedings*, 595(1):3–15, 2001.

[10] Franklin Chang-Diaz, Jared Squire, Roger Bengtson, Boris Breizman, Mark Carter, and F. Baity. *The physics and engineering of the VASIMR engine*.

[11] R.W. Boswell. Plasma production using a standing helicon wave. *Physics Letters A*, 33(7):457–458, 1970.

[12] RW Boswell and Christine Charles. The helicon double layer thruster. In *28th International Electric Propulsion Conference, IEPC*, 2003.

[13] C. Charles, R. W. Boswell, and M. A. Lieberman. Xenon ion beam characterization in a helicon double layer thruster. *Applied Physics Letters*, 89(26):261503, 2006.

[14] Benjamin W Longmier, Edgar A Bering, Mark D Carter, Leonard D Cassady, William J Chancery, Franklin R Chang Díaz, Tim W Glover, Noah Hershkowitz, Andrew V Ilin, Greg E McCaskill, Chris S Olsen, and Jared P Squire. Ambipolar ion acceleration in an expanding magnetic nozzle. *Plasma Sources Science and Technology*, 20(1):015007, jan 2011.

[15] D. F. Berisford, Roger D. Bengtson, and Laxminarayan L. Raja. Power balance and wall erosion measurements in a helicon plasma. *Physics of Plasmas*, 17(3):033503, 2010.

[16] Juan Del Valle, Jose Castro Nieto, Erick Chinchilla, Esteban Echeverría, Daniel Lezama, Carlos Martínez, Jorge Oguilve, Allan Rivera, Max Rodríguez, Juan Valverde, Rónald Díaz, Christopher Olsen, Andrew Ilin, Matthew Giambusso, Mark Carter, J. Squire, and Franklin Díaz. Measurement of the dielectric wall erosion in helicon plasma thrusters: an application to the vasimr® vx-cr experiment. 10 2013.

[17] A. Fruchtman. Electric field in a double layer and the imparted momentum. *Phys. Rev. Lett.*, 96:065002, Feb 2006.

[18] A. Fruchtman. The thrust of a collisional-plasma source. *IEEE Transactions on Plasma Science*, 39(1):530–539, 2011.

[19] A. Fruchtman. Neutral depletion in a collisionless plasma. *IEEE Transactions on Plasma Science*, 36(2):403–413, 2008.

[20] Eduardo Ahedo and Jaume Navarro Cavallé. Helicon thruster plasma modeling: Two-dimensional fluid-dynamics and propulsive performances. *Physics of Plasmas*, 20, 04 2013.

[21] Logan T. Williams and Mitchell L. R. Walker. Thrust measurements of a radio frequency plasma source. *Journal of Propulsion and Power*, 29(3):520–527, 2013.

[22] Adam Shabshelowitz and Alec D. Gallimore. Performance and probe measurements of a radio-frequency plasma thruster. *Journal of Propulsion and Power*, 29(4):919–929, 2013.

[23] Kazunori Takahashi, Daiki Sato, Koichi Takaki, and Akira Ando. Development of a compact magnetically expanding plasma source with a strong magnetic field. *Plasma Sources Science and Technology*, 22(5):055002, aug 2013.

[24] T. Lafleur. Helicon plasma thruster discharge model. *Physics of Plasmas*, 21(4):043507, 2014.

[25] Manuel Gamero-Castaño and Inna Katz. Estimation of hall thruster erosion using hphall. 2005.

[26] George-Cristian Potrivitu and Constantin Rotaru. Hall effect thruster erosion mechanism and the thruster lifetime. 10 2014.

[27] Eduardo Ahedo. Cylindrical model of a helicon-generated plasma. In *31th International Electric Propulsion Conference, Ann Arbor, Michigan, USA, IEPC*, volume 193, page 2009, 2009.

[28] T. Gronych, R. Ulman, L. Peksa, and P. Řepa. Measurements of the relative momentum accommodation coefficient for different gases with a viscosity vacuum gauge. *Vacuum*, 73(2):275–279, 2004. Proceedings of the European Vacuum Congress Berlin 2003, 23-26 June 2003, featuring the 8th European Vacuum Conference, 2nd Annual Conference of the German Vacuum Society.

[29] Donald Rapp and Paula Englander-Golden. Total cross sections for ionization and attachment in gases by electron impact. i. positive ionization. *The Journal of Chemical Physics*, 43(5):1464–1479, 1965.

[30] A V Phelps and Z Lj Petrovic. Cold-cathode discharges and breakdown in argon: surface and gas phase production of secondary electrons. *Plasma Sources Science and Technology*, 8(3):R21–R44, jan 1999.

[31] F J de Heer, R H J Jansen, and W van der Kaay. Total cross sections for electron scattering by ne, ar, kr and xe. *Journal of Physics B: Atomic and Molecular Physics*, 12(6):979–1002, mar 1979.

[32] M Hayashi. Determination of electron-xenon total excitation cross-sections, from threshold to 100 eV, from experimental values of townsend's . *Journal of Physics D: Applied Physics*, 16(4):581–589, apr 1983.

[33] James A. R. Samson and G. N. Haddad. Average energy loss per ion pair formation by photon and electron impact on xenon between threshold and 90 ev. *Radiation Research*, 66(1):1–10, 1976.

[34] Justin M. Little and Edgar Y. Choueiri. Thrust and efficiency model for electron-driven magnetic nozzles. *Physics of Plasmas*, 20(10):103501, 2013.

[35] Álvaro Sánchez-Villar, Jiewei Zhou, Eduardo Ahedo, and Mario Merino. Coupled plasma transport and electromagnetic wave simulation of an ECR thruster. *Plasma Sources Science and Technology*, 30(4):045005, apr 2021.

[36] F. Cannat, T. Lafleur, J. Jarrige, P. Chabert, P.-Q. Elias, and D. Packan. Optimization of a coaxial electron cyclotron resonance plasma thruster with an analytical model. *Physics of Plasmas*, 22(5):053503, 2015.

[37] K.-U. Riemann. The bohm criterion and the field singularity at the sheath edge. *Physics of Fluids B: Plasma Physics*, 1(4):961–963, 1989.

[38] K U Riemann. The bohm criterion and sheath formation. *Journal of Physics D: Applied Physics*, 24(4):493–518, apr 1991.

[39] K-U Riemann, J Seebacher, D D Tskhakaya, and S Kuhn. The plasma–sheath matching problem. *Plasma Physics and Controlled Fusion*, 47(11):1949–1970, oct 2005.

[40] R. Chodura. Plasma–wall transition in an oblique magnetic field. *The Physics of Fluids*, 25(9):1628–1633, 1982.

[41] I. I. Beilis, M. Keidar, and S. Goldsmith. Plasma-wall transition: The influence of the electron to ion current ratio on the magnetic presheath structure. *Physics of Plasmas*, 4(10):3461–3468, 1997.

[42] I. I. Beilis and M. Keidar. Sheath and presheath structure in the plasma–wall transition layer in an oblique magnetic field. *Physics of Plasmas*, 5(5):1545–1553, 1998.

[43] M. Keidar, I. D. Boyd, and I. I. Beilis. Plasma flow and plasma–wall transition in hall thruster channel. *Physics of Plasmas*, 8(12):5315–5322, 2001.

[44] E. Ahedo. Presheath/sheath model with secondary electron emission from two parallel walls. *Physics of Plasmas*, 9(10):4340–4347, 2002.

[45] D. L. Holland, B. D. Fried, and G. J. Morales. Sheath structure in a magnetized plasma. *Physics of Fluids B: Plasma Physics*, 5(6):1723–1737, 1993.

[46] Peter Sigmund. Theory of sputtering. i. sputtering yield of amorphous and polycrystalline targets. *Phys. Rev.*, 184:383–416, Aug 1969.

[47] J. Bohdansky. A universal relation for the sputtering yield of monatomic solids at normal ion incidence. *Nuclear Instruments and Methods in Physics Research Section B: Beam Interactions with Materials and Atoms*, 2(1):587 – 591, 1984.

[48] Yasunori Yamamura and Hiro Tawara. Energy dependence of ion-induced sputtering yields from monatomic solids at normal incidence. *Atomic Data and Nuclear Data Tables*, 62(2):149 – 253, 1996.

[49] M.A. Lieberman and A.J. Lichtenberg. *Principles of Plasma Discharges and Materials Processing*. Wiley, 2005.

[50] PC Zalm. Some useful yield estimates for ion beam sputtering and ion plating at low bombarding energies. *Journal of Vacuum Science & Technology B: Microelectronics Processing and Phenomena*, 2(2):151–152, 1984.

[51] J. Bohdansky, J. Roth, and H. L. Bay. An analytical formula and important parameters for low-energy ion sputtering. *Journal of Applied Physics*, 51(5):2861–2865, 1980.

[52] B Rubin, J L Topper, and A P Yalin. Total and differential sputter yields of boron nitride measured by quartz crystal microbalance. *Journal of Physics D: Applied Physics*, 42(20):205205, sep 2009.

[53] R. Gnizdor, K. Kozubsky, A. Koryakin, N. Maslennikov, S. Pridannikov, and M. Day. *SPT100 life test with single cathode up to total impulse two million NSEC.*

[54] C. Garner, J. C. Polk, K. Goodfellow, L. C. Pless, and J. Brophy. Performance evaluation and life testing of the spt-100. 1993.

[55] Sergey Khartov, Andrey Nadiradze, Olivier Duchemin, and Snecma Moteurs. Spt ceramic isolator surfaced layer composition change with lifetime. In *International Electric Propulsion Conference*, pages 2003–059, 2003.

[56] SA Khartov, AB Nadiradze, II Shkarban, and YV Zikeeva. Spt's high lifetime–some problems of solution. In *Proc. of the 29th In. Electric Propulsion Conf.–Princeton (USA).–2005.–9 p.(Paper № 2005-62)*, 2005.

[57] Shannon Y. Cheng and Manuel Martinez-Sanchez. Hybrid particle-in-cell erosion modeling of two hall thrusters. *Journal of Propulsion and Power*, 24(5):987–998, 2008.

[58] Sang-Wook Kim. *Experimental investigations of plasma parameters and species-dependent ion energy distribution in the plasma exhaust plume of a Hall thruster*. University of Michigan, 1999.

[59] Bryan Reid, Rohit Shastry, Alec Gallimore, and Richard Hofer. *Angularly-Resolved ExB Probe Spectra in the Plume of a 6-kW Hall Thruster.*

[60] Rohit Shastry, Richard R. Hofer, Bryan M. Reid, and Alec D. Gallimore. Method for analyzing e×b probe spectra from hall thruster plumes. *Review of Scientific Instruments*, 80(6):063502, 2009.

[61] Richard Hofer and David Jacobson. Development and characterization of high-efficiency, high-specific impulse xenon hall thrusters. 07 2004.

[62] Brian Beal. Clustering of hall effect thrusters for high-power electric propulsion applications. 01 2004.

[63] Jesse Allen Linnell. *An evaluation of krypton propellant in Hall thrusters*. PhD thesis, University of Michigan, January 2007.

[64] Vito Lancellotti, Riccardo Maggiora, Giuseppe vecchi, Daniele Pavarin, Simone Rocca, and Cristina Bramanti. *Radiofrequency Plasma Thrusters: Modelling Of Ion Cyclotron Resonance Heating And System Performance*.

[65] JA Castro Nieto, Juan Del Valle, Carlos Martınez, Allan Rivera, Jorge Oguilve, Christopher S Olsen, Matthew Giambusso, Mark D Carter, Jared P Squire, and Franklin R Chang Dıaz10. Vasimr® vx-cr experiment: status, diagnostics and plasma plume characterization. In *33rd International Electric Propulsion Conference, Washington, DC, USA*, pages 6–10, 2013.

[66] Eduardo Ahedo. Parametric analysis of a magnetized cylindrical plasma. *Physics of Plasmas*, 16(11):113503, 2009.

[67] James Gilland. Mission and system optimization of nuclear electric propulsion vehicles for lunar and mars missions. 01 1992.

[68] Eduardo Ahedo. Magnetic confinement of a high-density cylindrical plasma. *Physics of Plasmas*, 18(10):103506, 2011.

[69] Min Li, Hai-Bin Tang, Jun-Xue Ren, and Thomas M. York. Modeling of plasma processes in the slowly diverging magnetic fields at the exit of an applied-field magnetoplasmadynamic thruster. *Physics of Plasmas*, 20(10):103502, 2013.

[70] Kazunori Takahashi, Aiki Chiba, Atsushi Komuro, and Akira Ando. Axial momentum lost to a lateral wall of a helicon plasma source. *Phys. Rev. Lett.*, 114:195001, May 2015.

[71] Kazunori Takahashi, Christine Charles, and Rod W. Boswell. Approaching the theoretical limit of diamagnetic-induced momentum in a rapidly diverging magnetic nozzle. *Phys. Rev. Lett.*, 110:195003, May 2013.

[72] Yoshinori Takao and Kazunori Takahashi. Numerical validation of axial plasma momentum lost to a lateral wall induced by neutral depletion. *Physics of Plasmas*, 22(11):113509, 2015.

[73] J Hopwood. Planar RF induction plasma coupling efficiency. *Plasma Sources Science and Technology*, 3(4):460–464, nov 1994.

[74] Benjamin W Longmier, Leonard D Cassady, Maxwell G Ballenger, Mark D Carter, Franklin R Chang-Díaz, Tim W Glover, Andrew V Ilin, Greg E McCaskill, Chris S Olsen, Jared P Squire, et al. Vx-200 magnetoplasma thruster performance results exceeding fifty-percent thruster efficiency. *Journal of Propulsion and Power*, 27(4):915–920, 2011.

[75] Charles A. Lee, Guangye Chen, Alexey V. Arefiev, Roger D. Bengtson, and Boris N. Breizman. Measurements and modeling of radio frequency field structures in a helicon plasma. *Physics of Plasmas*, 18(1):013501, 2011.

[76] F. F. Chen and R. W. Boswell. Helicons-the past decade. *IEEE Transactions on Plasma Science*, 25(6):1245–1257, 1997.

[77] H N Kucukarpaci and J Lucas. Electron swarm parameters in argon and krypton. *Journal of Physics D: Applied Physics*, 14(11):2001–2014, nov 1981.

[78] P. C. Stangeby. The bohm–chodura plasma sheath criterion. *Physics of Plasmas*, 2(3):702–706, 1995.

[79] K.-U. Riemann. The validity of bohm's sheath criterion in rf discharges. *Physics of Fluids B: Plasma Physics*, 4(9):2693–2695, 1992.

[80] Zhu Lin Zhang and Lai Zhang. Anisotropic angular distribution of sputtered atoms. *Radiation Effects and Defects in Solids*, 159(5):301–307, 2004.

[81] Y. Garnier, V. Viel, J.-F. Roussel, and J. Bernard. Low-energy xenon ion sputtering of ceramics investigated for stationary plasma thrusters. *Journal of Vacuum Science & Technology A*, 17(6):3246–3254, 1999.

[82] C. Lee and M. A. Lieberman. Global model of ar, o2, cl2, and ar/o2 high-density plasma discharges. *Journal of Vacuum Science & Technology A*, 13(2):368–380, 1995.

[83] Shinatora Cho, Kimiya Komurasaki, and Yoshihiro Arakawa. Kinetic particle simulation of discharge and wall erosion of a hall thruster. *Physics of Plasmas*, 20(6):063501, 2013.

[84] Justin Little and Edgar Choueiri. *The Influence of Induced Currents on Magnetic Nozzle Acceleration and Plasma Detachment.*

[85] K Dannenmayer and Stéphane Mazouffre. Electron flow properties in the far-field plume of a hall thruster. *Plasma Sources Science and Technology*, 22(3):035004, apr 2013.

[86] J. M. Little and E. Y. Choueiri. Electron cooling in a magnetically expanding plasma. *Phys. Rev. Lett.*, 117:225003, Nov 2016.

[87] Ioannis G. Mikellides, Pavlos G. Mikellides, Peter J. Turchi, and Thomas M. York. Design of a fusion propulsion system-part 2: Numerical simulation of magnetic-nozzle flows. *Journal of Propulsion and Power*, 18(1):152–158, 2002.

[88] Álvaro Sánchez-Villar, Jiewei Zhou, Eduardo Ahedo, and Mario Merino. Coupled plasma transport and electromagnetic wave simulation of an ECR thruster. *Plasma Sources Science and Technology*, 30(4):045005, apr 2021.